



Electron Backscatter Diffraction Technique: Fundamentals to Applications

Shashank Shekhar, Nitin Kumar Sharma, Sandeep Sahu,
and Santanu Misra

1 Introduction

Orientation imaging microscopy (OIM) has long been the quest of material scientists and microscopists, as it provides an immense amount of quantitative data about the microstructure of a material, which can then be related to its processing and also to the performance of the component. There are several techniques which can provide orientation information, some of which are electron channeling contrast imaging (ECCI) in SEM to convergent beam electron diffraction (CBED) and selected area diffraction (SAD) in transmission electron microscope (TEM). Each of these techniques is good in themselves in providing orientation; however, each of them is beset by some drawbacks which have subdued their utilization. A major limitation of these techniques is that they are not suitable for automation which allows to obtain orientation data from various points on a large scanned area. However, it must be pointed out that TEM-based EBSD has also now gained traction and it is gaining applicability among researchers.

In simple terms, electron channeling contrast is obtained due to difference in density of atoms along different directions, which results in varied intensity of backscattered electrons (BSEs) (Joy et al. 1982; Wilkinson and Hirsch 1997; Zaefferer and Elhami 2014). A schematic to explain this effect is shown in Fig. 1. If the electron beam is rastered in two-dimensional space of the sample surface, then one can expect that several lattice planes would together

contribute to the electron contrast. One can expect high contrast from planes which are close to normal to the surface, while those away from the normal would show low contrast. Overall, backscattered beam would have a contrast in the form of bands, which carry information about orientation and lattice defects. The bands reflect the inherent symmetry of the orientation of the point, while local features reflect defects in the lattice. Coates was the first person to obtain patterns based on this technique (Coates 1967). This technique is not easy to automate because accurate and automated rocking of beam is not allowed in most electron microscopes. Moreover, the beam rocking process is very slow, and hence getting scans from a large number of points makes the process tedious (Kamaladasa and Picard 2010). Nonetheless, this process has been very successful in understanding lattice defects (Zaefferer and Elhami 2014; Ahmed et al. 1997).

In TEM, when thin foils are subjected to high-energy parallel beam, it leads to diffraction due to lattice points. If the beam illuminates a single crystal, then various planes of the crystal diffract to produce pattern of points. The symmetry and orientation of these points can be directly related to the orientation of the crystal and hence can be used for orientation imaging microscopy. A schematic of the process and the pattern obtained is shown in Fig. 2. Another related technique is convergent electron beam diffraction, which utilizes convergent beam, instead of parallel beam, and results in disks, instead of points in the diffraction pattern. This, too, can be used for understanding the orientation of the crystal.

Orientation recognition from SAD pattern has been commercialized, and it has also become a good tool for orientation imaging microscopy, particularly when the grains or precipitates are small in size.

S. Shekhar (✉) · S. Sahu
Grain Boundary Engineering Lab, Materials Science and
Engineering, IIT Kanpur, Kanpur, UP 208016, India
e-mail: shashank@iitk.ac.in

N. K. Sharma
Chemical and Materials Engineering, University of Alberta,
Edmonton, AB T6G 21, Canada

S. Misra
Department of Earth Sciences, IIT Kanpur, Kanpur, UP 208016,
India

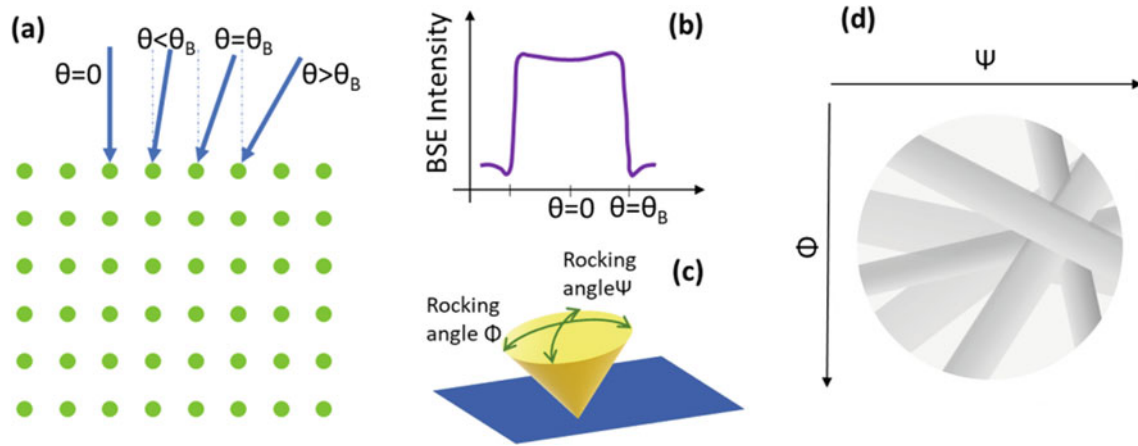
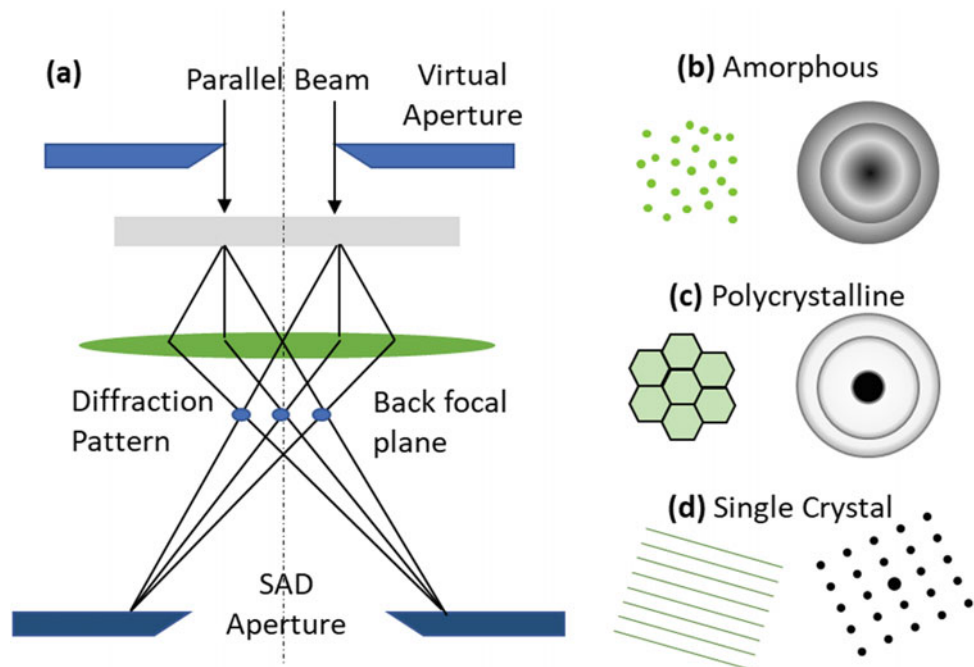


Fig. 1 **a** Orientation variation of incoming beam. **b** Its effect on BSE intensity. **c** Rocking of beam in 2 directions. **d** Schematic of the generated ECCI pattern. **a** and **b** adapted from Wilkinson and Hirsch (1997)

Fig. 2 **a** Schematic of the SAD pattern generation in TEM and the diffraction pattern corresponding to **b** amorphous material. **c** Polycrystalline material. **d** Single crystalline material



2 Origin of Kikuchi Pattern

Kikuchi pattern was first observed by S. Nishikawa and S. Kikuchi in 1928 during diffraction of cathode rays by calcite (Nishikawa and Kikuchi 1928a,b). In one of these publications, they presented transmission Kikuchi patterns (TKPs) (Nishikawa and Kikuchi 1928b), and in the other, they presented backscatter Kikuchi patterns (BKPs) (Nishikawa and Kikuchi 1928a). While most of the work in the early phase was concentrated on transmission Kikuchi diffraction (TKD), last three decades have seen a lot of attention being given to SEM-based backscatter Kikuchi diffraction, which

has widely come to be known as electron backscatter diffraction (EBSD). It has further gained prominence due to automation and improvement in hardware which have accelerated acquiring and analyzing speed of these Kikuchi patterns (Kunze et al. 1993).

Kikuchi patterns are formed by the backscattered electrons that satisfy the diffraction condition for a given set of planes. A schematic of the same is shown in Fig. 3. When the electron beam falls on the material, interaction of electron and atoms takes place, and scattering of the incoming electrons occurs. The point of scatter becomes the source of secondary waves which has varying intensity at different orientations. Now, these secondary waves of electrons can

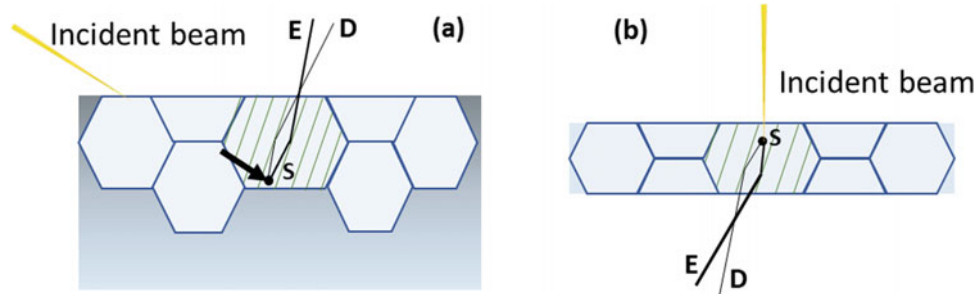


Fig. 3 Schematic showing generation of **a** backscatter Kikuchi diffraction in a bulk sample and **b** transmission Kikuchi diffraction in a thin foil ('S' is the scattering event which acts as source, 'D' is part of the defect cone, and 'E' is part of the excess cone)

further interact with the lattice points and result in diffraction, very similar to that in X-ray diffraction. One major difference with X-ray diffraction, however, is that wavelength of the electron waves is very small, leading to a very small Bragg's angle (θ) in Bragg's equation, $n\lambda = 2d \sin \theta$. For the sake of comparison, wavelength of $K\alpha$ radiation originating from Cu source during X-ray diffraction is $\sim 1.54 \text{ \AA}$. On the other hand, wavelength of electron at 10 kV accelerating voltage is $\sim 0.12 \text{ \AA}$. Since the wavelength of these electron waves is an order of magnitude smaller than that of X-rays, Bragg's angles also come out to be much smaller than that obtained in X-ray diffraction.

Another major difference with X-ray diffraction is that since the 'source' of electrons is inside the material, diffraction may take place in 'forward' as well as 'backward direction,' as depicted in the schematic. Thus, in this diffraction, there is always a pair of diffracted cones. When these cones intersect with a planar detector, we observe a pair of hyperbolae. But due to the small values of Bragg angles, the curvatures of these hyperbolae are so small that they appear as parallel lines. These parallel lines are known as Kikuchi lines or Kikuchi bands. Because of the nature of its origin, one of the cones has higher intensity than the background, while the one which diffracted from the backward moving waves has intensity lower than the background. Thus, we obtain what are called as 'defect cone' and 'excess cone.' These cones and corresponding Kikuchi lines are formed in both transmission mode and backscatter mode. The geometry of the two modes is somewhat different and would be discussed in next section.

Since the Kikuchi patterns are formed by a fundamental phenomenon of diffraction, they show certain characteristics that help in understanding the structure and orientation of material. Each band in the Kikuchi pattern represents diffraction from a family of planes. Thus, each band has a one-to-one relation with family of planes. This, in turn, implies that intersection of these bands represents intersection of planes, viz. zone axes. Moreover, angle between the bands represents angle between planes. These characteristics of the Kikuchi pattern are exploited to identify the

orientation of the individual point of the sample. In scanning electron microscope (SEM), the beam rasters over a region, moving from point to point in a serpentine fashion. Thus, one can obtain orientation of each of these points and recreate a micrograph representing the orientation map of the scanned region. Another important characteristic of these patterns is that the width of each of the bands is proportional to the spacing of the planes of that family. It can be easily shown that the angular separation between the two parallel lines of the Kikuchi band is twice the Bragg angle. From this, it can be extrapolated that if there are defects in the material which can cause variation in the average planar spacing, then it would reflect in the bands. This characteristic has also been exploited in EBSD to quantify the strain in the lattice (Wilkinson and Britton 2012).

3 Automated Indexing of Kikuchi Patterns

We pointed out earlier that application of EBSD has seen an exponential growth in last two decades. This is driven primarily by automation of pattern indexing across a selected grid in the scan area. This automation has allowed indexing of patterns from area as large as several $100 \mu\text{m}$ along both the directions. Automatic indexing has been achieved on the foundation of improvement in software as well as hardware capabilities. On the hardware front, there is a phosphor screen on which the Kikuchi patterns are formed, and the illuminated pattern is captured by a camera that is located behind this screen. The capabilities of the camera and screen have improved immensely over the years, so that the screen capturing rate has reached in excess of 2500 frames per second. Faster scanning rate has resulted in obtaining large maps in very short times. Once the images are captured, they are analyzed to identify the orientation and phase of the given point. In the next few paragraphs, we explain the method of recognition of Kikuchi pattern and indexing of the orientation of a given point from the obtained Kikuchi pattern.

Once the camera captures the Kikuchi pattern, identification of various lines from the Kikuchi pattern is carried out

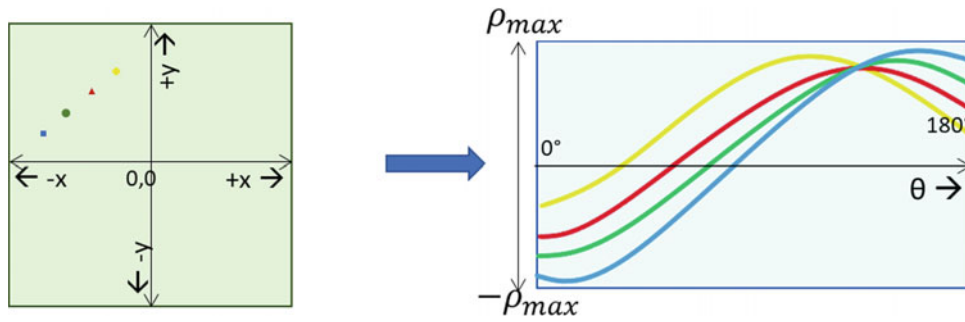


Fig. 4 Hough transformation translates each pixel in image space to a curve in the ' ρ - θ ' space, and consequently, a line in the image space appears as an intersection of several of these curves in the ' ρ - θ ' space

using Hough transform. In this technique, the line is transformed from Cartesian coordinate to a space where it is represented only by its length ' ρ ' and angle ' θ '. To understand this, let us imagine a square image containing just one line. If we want to transform each pixel of this image space into ' ρ ' and ' θ ' parameter space, then each pixel on the image would transform to a sinusoidal curve in the ' ρ - θ ' space. This is because each pixel can be imagined to be a part of infinite number of straight lines passing through it. Set of these straight lines would form a curve as represented in Fig. 4 (left). Now, wherever a line exists in image space, it will be represented as intersection of several of these sinusoidal curves at one point, as shown in Fig. 4 (right). This intersection point in the ' ρ - θ ' space has value of ' ρ_i ' and ' θ_i ' which represents the given line in the image space. In the present context, ' ρ ' varies from ' $-\rho_{\max}$ ' to ' ρ_{\max} ' and ' θ ' varies from 0 to 180°. Now, if we assign intensity value to each of these pixels in image space, then the intensity value of this particular ' ρ_i ' and ' θ_i ' would be much higher than that of its neighborhood. When all of Kikuchi pattern is transformed into ' ρ - θ ' space, this is called Hough transformation. In the Hough transformed image, third direction represents the intensity, and each straight line in image space is represented by a 'Hough' or a mound, which has relatively higher intensity value compared to its neighbor. The bright lines can be easily identified by the relatively large peaks in the Hough transform space. Once these lines are identified, calculating the angle between the planes is much easier in this ' ρ - θ ' space, as one can easily identify the equation for each and every line which is given as: $\rho_i = x \cos \theta_i + y \sin \theta_i$.

Kikuchi pattern is a set of bands with parallel lines, and each of these bands represents a family of planes of the crystal structure of the given phase. The centerline of each of these bands represents the trace of orientation of the given family of planes. Hence, by identifying the lines, as described in the previous paragraph, and by calculating the angle between any pair of bands, we are essentially calculating the angle between corresponding pair of family of planes. This

angle between various sets of planes can be compared to the reference values of the crystal structure of the possible phases. At least 3 different sets of mutually intersecting lines and their corresponding angles must match, to uniquely identify the phase and define the crystal orientation of the point on the crystal. In general, 5 to 8 bands or reflectors need to be matched to get confidence in the result and to improve the accuracy of the orientation.

4 Geometry of EBSD Setup

In EBSD, it is very important to understand the geometry of the setup so that appropriate corrections can be made for the geometry during analysis. Intensity of the backscattered electrons has an angular distribution, and this angular distribution is also dependent upon the angle of incidence of the electron beam on the sample (Berger and Niedrig 1999). When the electron beam falls normally to the sample surface, highest intensity of the backscattered electrons lies normal to the plane. However, this distribution is very different when the electron beam has an acute incidence angle. A schematic of the angular density of the backscattered electrons in these two cases is shown in Fig. 5. In general, it is found that maximum intensity is found at an angle which is equal to the angle of incidence of the beam on the sample, as shown in the schematic (Berger and Niedrig 1999). Ideally, one would like to keep the sample normal and the detector right at the pole piece. However, due to constraints of space this is not feasible, and the next best configuration is to keep the sample oriented at some steep angle and keep the detector where one can get the maximum intensity of backscattered electrons. EBSD researchers have found that yield of the backscattered electron is highest at 70° tilt. The overall geometry of the sample with respect to the EBSD detector and the pole piece is shown in Fig. 6a. Figure 6b shows a typical Kikuchi pattern. This particular pattern was obtained from a single-phase material with FCC crystal structure at an accelerating voltage of 20 kV.

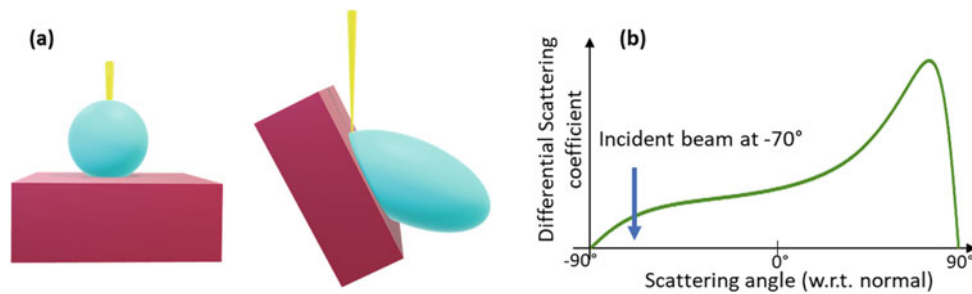


Fig. 5 **a** Schematic representation of the three-dimensional angular distribution of backscatter electrons. **b** Schematic representation of variation of differential scattering coefficient with scattering angle, assuming sample has a 70° tilt. Adapted from Berger and Niedrig (1999)

The tilted sample geometry has a significant role on the overall spatial resolution and also the fact that the lateral resolution is different from the longitudinal resolution of the scanned sample. Figure 7a shows the schematic interaction of the beam with the sample. The depth from which backscattered electrons can escape the surface to reach the detector is denoted by d_z . Its absolute value depends on the accelerating voltage and the atomic number of the given material. In general, its value ranges from 50 to 100 nm, which is a very small depth. This also implies that the surface must be polished and must be free of any asperities at least up to this depth. If there are any remnant strains or scratches due to polishing which are of this order, then obtaining Kikuchi pattern is not possible. This also explains why sample preparation is a very delicate and dedicated step for EBSD. There is dedicated equipment that has been designed in the past few decades, particularly for the preparation of the samples for EBSD. Some of the dedicated equipment is vibratory polishing machine and electropolishing machine.

In Fig. 7a, the largest cross section of the teardrop interactive volume represents the spatial resolution in lateral and longitudinal directions. It is obvious from the figure that this cross-sectional area is much larger than the spot size of the beam. A larger cross section also suggests that the yield of the backscattered electrons would be high. Secondly, it is also clear that due to the tilt of the sample, longitudinal resolution d_y is much larger (poorer) than the lateral resolution d_x . On a first order of approximation, it can be said that $d_y = d_x / \cos \theta$, based on the geometry of the sample, which is tilted at an angle θ from the direction of the electron beam. A schematic of the variation of lateral and longitudinal resolution with change in accelerating voltage is shown in Fig. 7b. The absolute values of resolution can range from 50 nm to few μm . By applying very low accelerating voltages, researchers have achieved resolution as low (good) as 10 nm (Dingley et al. 2005; Chen et al. 2011). This improvement is achieved as the interaction volume decreases with decrease in accelerating voltage.

The fact that resolution is dependent upon the geometry of sample and the interaction volume has been exploited for transmission Kikuchi diffraction in SEM. Here, like in TEM, a thin foil is used whose interaction volume is very small, and thus, the resolution is also small (better). A schematic of the same is shown in Fig. 8. In effect, the resolution is as good as the spot size of the beam falling on the sample can be obtained using this geometry. Resolution up to a few nm can be obtained using this technique (Wang et al. 2016).

5 Data Acquisition Parameters

Previous sections clearly outline the theory that lies behind EBSD-based OIM. Like any experimental technique, there are several other parameters related to hardware and software that need to be optimized in order to obtain good-quality data. In this section, we will discuss some of these important parameters and what points to keep in mind when acquiring data. First and foremost step in good-quality data acquisition is sample preparation. As pointed out earlier, during EBSD, data is acquired from only up to a depth of 50–100 nm from sample surface. This puts a huge obligation of preparing a surface that is free from any polishing artifacts up to a depth of few 10's of nm. However, we will not delve into sample preparation here, and readers are directed to read some of these in-depth studies on sample preparation for EBSD (Wang et al. 2016; Nowell et al. 2005; Michael and Giannuzzi 2007).

Once the Kikuchi patterns from a well-prepared sample are discernible, then the objectives of the users are to obtain high accuracy data and at high frame rate. High accuracy refers to high probability of getting correct identification of the orientation, and high frame rate refers to acquisition of a large number of frames and its analysis per unit time. Both these sets of objectives require different sets of parameters, and hence, there is a need to optimize them. The SEM operating condition should be set such that the current in the SEM is on the higher side. This is particularly true for FESEMs as the total

Fig. 6 **a** Geometry of the sample with respect to the incident beam and the EBSD detector (PC refers to pattern center). **b** A Kikuchi pattern obtained from a single-phase FCC crystal

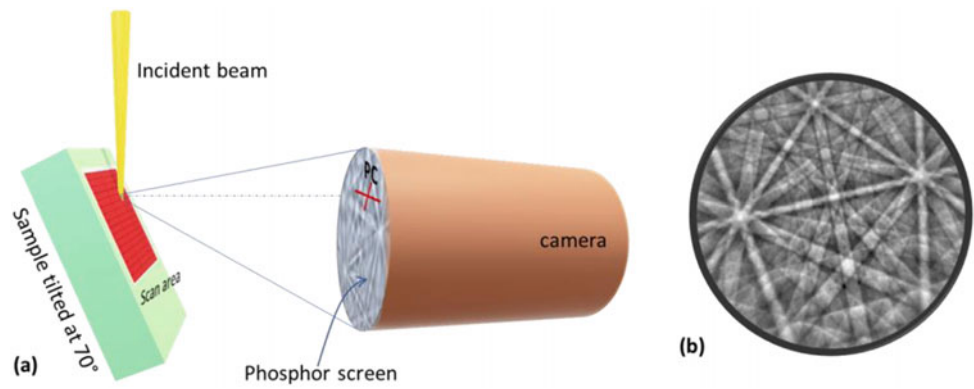


Fig. 7 **a** Schematic representation of interaction of beam with the sample in backscatter diffraction mode, also showing the largest cross section from which backscatter electrons escape. **b** Schematic of the variation of lateral and longitudinal resolution with change in accelerating voltage

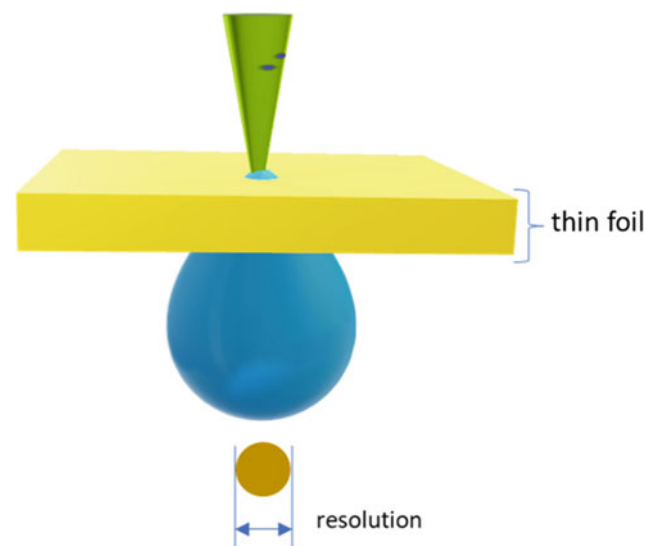
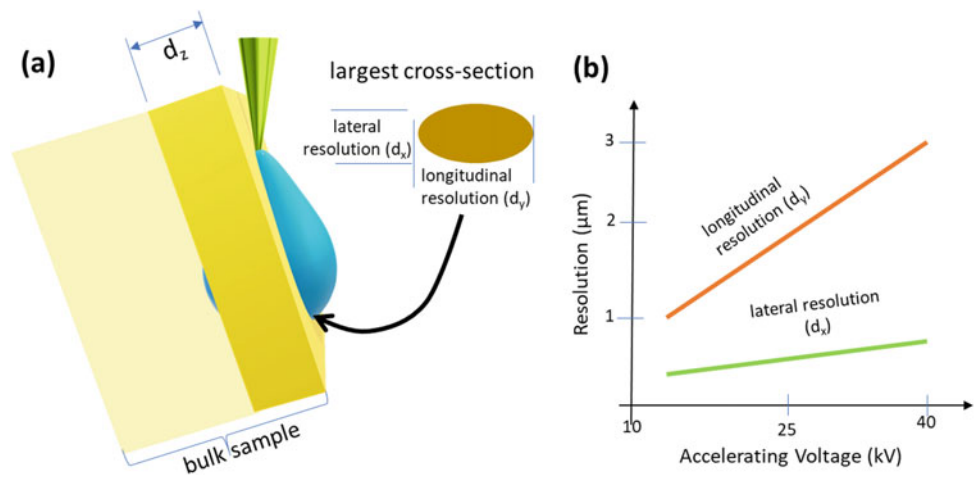


Fig. 8 Schematic representation of interaction of beam with thin foil in transmission Kikuchi diffraction mode. Also showing the large cross section, which represents the resolution of the geometry

current in field emission SEMs is quite low. Good current is necessary for obtaining high-contrast diffraction bands. The accelerating voltage has direct implication on the resolution of

data, and it is usually kept at 10 kV. For resolving small particles, one may need to reduce the accelerating voltage to much lower values (Singh et al. 2018).

In the data acquisition window, we get to optimize the contrast of the patterns again, using gain and exposure time. Increasing the gain improves the signal, but the signal-to-noise ratio also deteriorates. On the other hand, increasing the exposure time improves signal as well as signal-to-noise ratio, but the acquisition rate goes down. Additionally, the gain needs to be just sufficient so that there is no saturation in the signal. Another important parameter that affects pattern quality and image acquisition rate is the binning size of the Kikuchi pattern. Usually, the Kikuchi pattern is obtained as a high-resolution image (e.g., 1024×1024 pixels). The binning size refers to the number of pixels that would be averaged when analyzing the Kikuchi pattern. Thus, a 1×1 binning would imply that all the 1024×1024 pixels (1,048,576 pixels) would be analyzed. However, a 4×4 binning would imply that only 65,536 pixels would be analyzed. This greatly reduces the analysis time, and hence, the acquisition rate increases drastically. The downside is that this also leads to reduced resolution of the Kikuchi pattern, and hence, it may

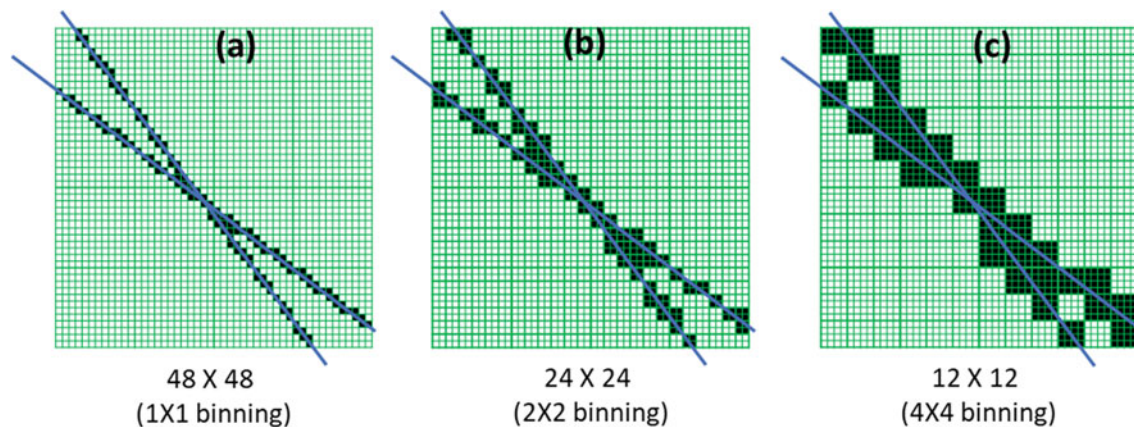


Fig. 9 Effect of binning size on the resolution of the image: Two straight lines are drawn on a grid of 48×48 at three different binning sizes. **a** 1×1 binning. **b** 2×2 binning. **c** 4×4 binning

deteriorate the accuracy. This is explained schematically in Fig. 9. Depending on the material and the polishing condition, one needs to identify the highest binning that can give accurate results and thus improve the acquisition rate. Data acquisition software also allows the user to improve the image contrast by subtracting background signal. Background signal refers to the signal being received from several other neighboring grains that can reduce the overall image contrast. By subtracting or dividing this background signal from the obtained signal, the contrast of the pattern obtained from the immediate point is improved significantly.

Once the pattern acquisition parameters are set, the user needs to define the step size for the scan area. Step size is the distance between two consecutive points from which orientation is obtained and thus defines the total number of points that will be acquired in a given scan area. If the step size is very small, one would be able to get very high-resolution micrograph with no visible jig-jag-type structure in the grain boundary; however, this also implies a significantly longer time to acquire the image. Usually, the electron beam inside the SEM has a gradual drift, and for very large scans, the total beam drift may be too large, and the OIM micrograph would yield elongated structures. On the other hand, using a very large step size takes very short time, albeit it sacrifices resolution. In fact, some very small grains may not get detected if the step size is too large. Hence, it is imperative to select an optimal step size. As a rule of thumb, step size should be taken as grain size divided by 10. This would yield on an average 100 points per grain, and the scan speed would also not be compromised. However, if the micrograph consists of very fine grains, then one has to ensure that all these grains are captured. Another rule of thumb is that at least 10 pixels should be present in a region for it to be defined as grain. So, this serves as another guide in selecting the step size. The users should also be aware of the smallest step size that yields meaningful result in their respective SEM. As a point of reference, the smallest

step size that gives meaningful result using the Oxford Instruments' Nordlys EBSD detector installed in the FESEM JEOL JSM-7100F in the ACMS facility at IIT Kanpur is 50 nm. This would imply that the smallest grain that can be detected would have an area of $10 \text{ pixels} \times (0.05 \mu\text{m})^2$, which is approximately $0.025 \mu\text{m}^2$ or a square with $\sim 158 \text{ nm}$ length.

6 Data Analysis

In the earlier sections, we discussed the theory of electron backscatter diffraction, and then we discussed the data acquisition process and the important parameters to keep in mind in order to obtain high-quality data at fast scan rates. Next, we need to understand how to interpret this data so that quantitative microstructural information can be extracted. Later, we will provide some case studies where these analyses are put in application. Data that is acquired from the EBSD acquisition software is simply the crystal orientation data for each and every point. Next few paragraphs will elaborate how this information alone is sufficient to extract quantitative information about several microstructural parameters. Some additional data is also collected at each point, which aids in analyzing and quantifying results. EBSD pattern at each point can also be saved, and these are used in special cases to analyze the results to a greater depth. First and foremost, we need to understand what is the mathematical form of these orientations and what is the reference frame with respect to which this orientation data is gathered.

6.1 Orientation Analysis

Orientation is always defined with respect to some reference coordinate. In this sense, orientation is the rotation from the

specimen coordinate system to crystal coordinate system. Mathematically, this can be described by rotation vector 'g'. A schematic is shown in Fig. 10a which represents orientation as rotation from specimen coordinate system to crystal coordinate system. Usually, the three primary orientations of sample coordinate system are denoted as 'rolling direction,' 'normal direction,' and 'transverse direction,' and three coordinates of the crystal are defined by $\langle 100 \rangle$, $\langle 010 \rangle$, and $\langle 001 \rangle$. Another way of representing orientation or transformation is using the Euler angles, which is defined in terms of three angles $(\varphi_1, \theta, \varphi_2)$. These sets of angles are also called yaw, pitch, and roll and are explained in Fig. 10b. It can be readily shown that the rotation matrix 'g' and the Euler angles are related by the following equation:

$$g = \begin{pmatrix} \cos \varphi_1 \cos \varphi_2 - \sin \varphi_1 \sin \varphi_2 \cos \theta & \sin \varphi_1 \cos \varphi_2 + \cos \varphi_1 \sin \varphi_2 \cos \theta & \sin \varphi_2 \sin \theta \\ -\cos \varphi_1 \sin \varphi_2 - \sin \varphi_1 \cos \varphi_2 \cos \theta & -\sin \varphi_1 \sin \varphi_2 + \cos \varphi_1 \cos \varphi_2 \cos \theta & \cos \varphi_2 \sin \theta \\ \sin \varphi_1 \sin \theta & -\cos \varphi_1 \sin \theta & \cos \theta \end{pmatrix}$$

It is also possible to obtain the Euler angles from the rotation matrix 'g' (Herter and Lott 1993; Shoemaker 1994). There are some more mathematical ways of representation of orientation and the misorientation between the points, e.g., Rodrigues vector and quaternions (Heinz and Neumann 1991; Morawiec and Field 1996). We will not get into details of other kinds of representation, and for now, it is sufficient to understand that orientations can be represented in mathematical form and that they can be stored in terms of the above-mentioned parameters. We should also realize that

each of these representations is interchangeable, and one can get orientation parameters of one type of representation from other forms of representation.

With orientation data for each point of scan area, one can generate an orientation map giving unique color to each orientation. An easy way to define unique color to each orientation is by using a standard inverse pole figure (IPF) triangle of the crystal structure, with three primary colors (red, green, and blue) at three corners (Nolze and Hielscher 2016). The intermediate points are represented by a mix of these primary colors. Since the IPF represents all the possible orientations of a crystal, the colors provide an easy guide to the orientation of various points in the map. One such pseudo-colored orientation map, where each

point was assigned a color based on the color of the corresponding orientation in the inverse pole figure (also shown), is depicted in Fig. 11a. An Inconel-718 sample was taken for this scan, which was found to be single phase. Usually, Inconel contains several precipitates, but this particular sample was processed such that it was mostly single phase. Regions or domains with similar colors depict points with similar orientation and hence represent one crystallite or one grain. Black dots represent points from where Kikuchi pattern could not be obtained or could not be indexed. This scan

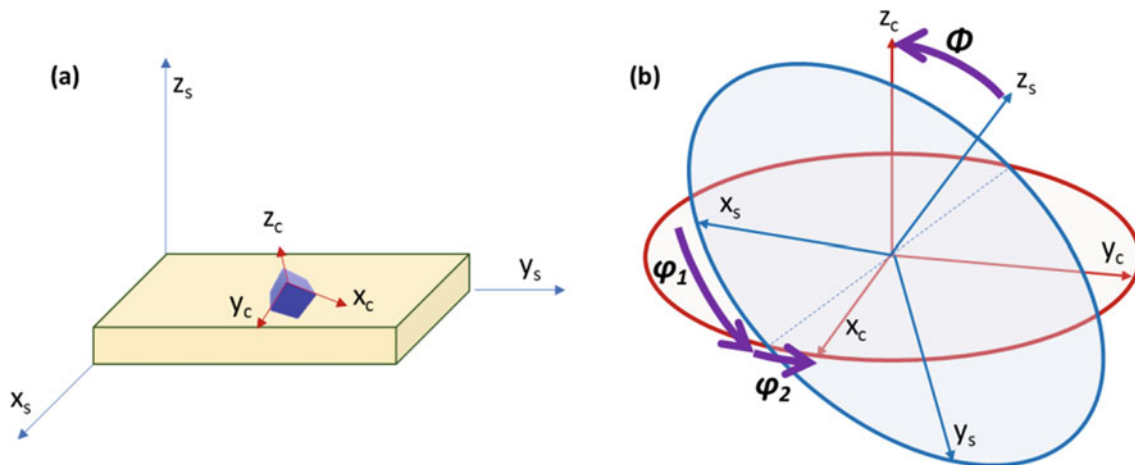


Fig. 10 Orientation of an individual crystal in a sample. **a** Crystal coordinate system (x_c, y_c, z_c) is described with respect to sample coordinate system (x_s, y_s, z_s) . **b** This rotation can achieve three

consecutive rotations, performed about the z_s -, x' -, and z'' -axes by magnitude φ_1, θ , and φ_2 , respectively

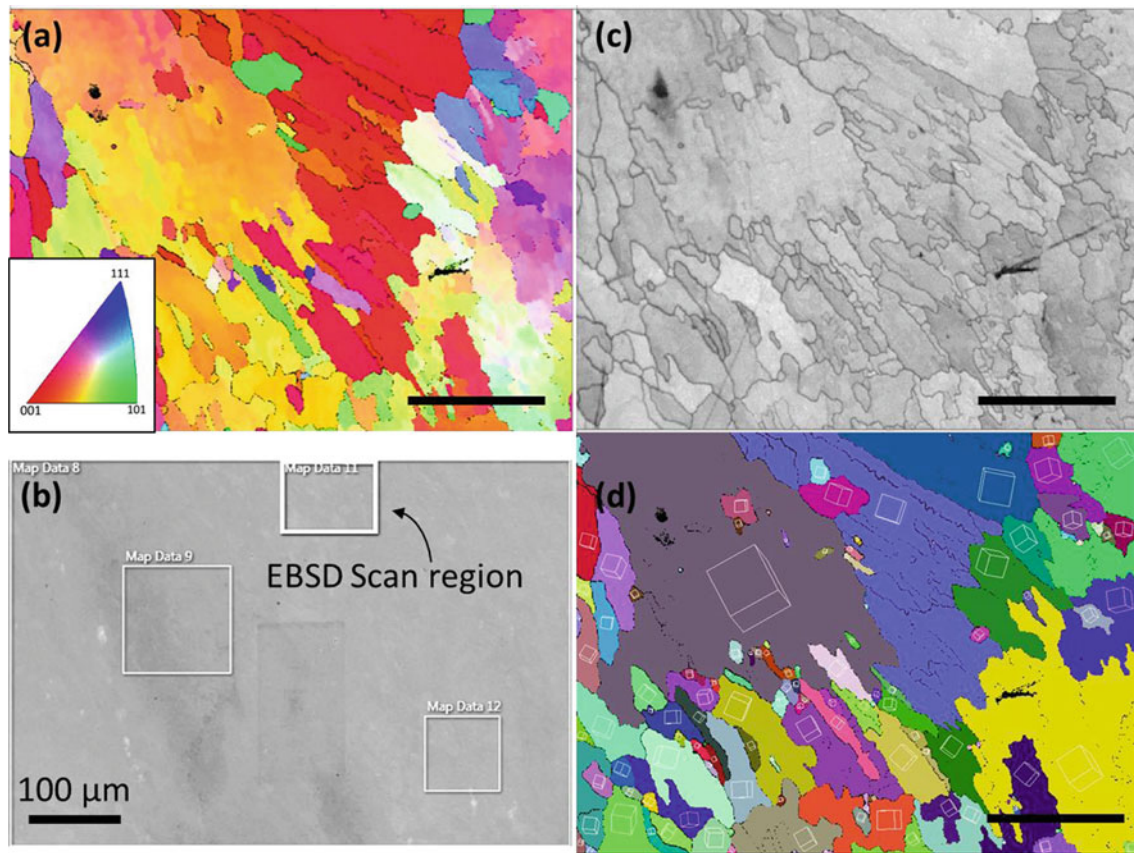


Fig. 11 EBSD of Inconel 718 sample. **a** Orientation map based on pseudo-colors of IPF (shown in inset). **b** SEM micrograph showing the region from where EBSD scan was taken. **c** Band contrast map. **d** Random colored grain map (scale bar = 25 μm , where not mentioned)

was taken with a step size of 150 nm over an area of $100 \times 75 \mu\text{m}$. This translates to 667 points along the horizontal direction and 500 points along the vertical direction, giving a total of 333,500 points to generate the orientation map. The reference inverse pole figure of cubic crystal structure with its color scheme is also shown in the inset. SEM micrograph of the material is also shown in Fig. 11b for reference, and the region from which scan was taken is marked on the SEM micrograph.

Another very useful map that is almost always generated using EBSD analysis tools is called band contrast map or pattern quality map, depending upon the manufacturer of the instrument. The primary information displayed in these maps is the contrast or average intensity of the Kikuchi bands for each and every point. If the sample is stress-free and generates good Kikuchi pattern, then these points will appear bright. On the other hand, points which are deformed or strained or cannot generate Kikuchi pattern for any other reason appear dark. The map so generated gives an idea about which regions contain defects and which regions are defect-free. Thus, this map can also be equated with the bright field image of TEM where defects usually appear darker relative to the brighter strain-free region. Band

contrast map of the above-mentioned sample is also presented in Fig. 11c. Based on similar orientation, grains can be demarcated and random color is assigned to them. This is called random colored grain map, as shown in Fig. 11d.

In microstructural analysis, identification of grains, size, and morphology is a very important parameter. However, orientation map based on IPF color scheme is not sufficient to differentiate between grains. There is a possibility that two grains have similar normal orientation, but they differ in azimuthal orientation; thus, they will be assigned similar colors and hence may seem to be part of the same grain. An example from the EBSD map, discussed above, is shown in Fig. 12. In such cases, Euler maps can be used as a handy tool. Euler maps assign color to different points based on the value of one of the Euler angles. Since there are three different Euler angles to define an orientation, thus there are three different kinds of Euler maps that can be generated. These maps can be used in conjunction with IPF maps to differentiate between grains. However, Euler maps have their own limitations, and other means are needed to identify and quantify information about grains.

Since EBSD is able to extract information about points which have similar orientation and hence form a grain, its

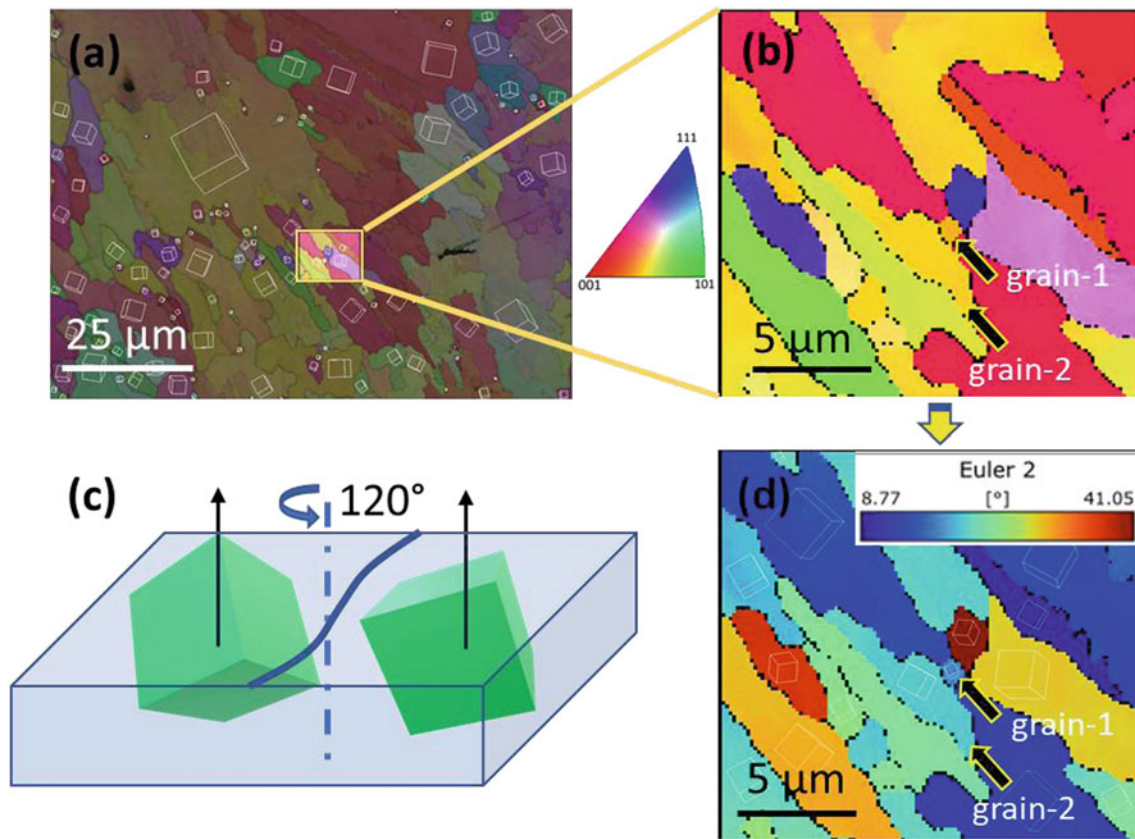


Fig. 12 **a** A small region from the orientation map is highlighted. **b** Orientation map of the highlighted region showing the two grains (grain-1 and grain-2) with similar color. **c** Two different grain scans

have same IPF color because they may have same normal orientation, but different azimuthal angles. **d** Additional information from Euler map helps in differentiating between the grains

analysis engine can identify the grains and even add unique random color to each of them. It must be noted that this color is not based on the orientation of the grains or Euler angles, but a random unique color so as to be able to identify them easily. A map with grains in random color is also presented in Fig. 11d. Each of these grains has a particular orientation of the crystallite, and it has been superimposed on the map showing the grains. At this point, it is important to caution the readers that grains in EBSD are not exactly the same as grains understood in metallography. In EBSD, grains are defined mathematically, and hence, one has to define the cutoff misorientation between grains. As long as two neighboring points have misorientation below this critical value, they will be considered part of the same grain, and when they have misorientations greater than this cutoff value, then the two points will be considered as part of two different grains. Usually, this cutoff is taken as 10° , and the random grain map shown in Fig. 11d is based on this definition. A grain may also be composed of some ‘sub-grains’ where the misorientation between the different parts is less than 10° , and when the grain definition is changed to a small value, say 2° , some of these ‘grains’ may start to appear. Band contrast map of a selected region of the original map is

shown in Fig. 13a. Figure 13b and c shows random grain maps with 10° grain definition and 2° grain definition, respectively. It is obvious from the figure that when the grain definition is reduced, lot more grains ‘appear,’ and some of these are highlighted in the figure. Grain statistics obtained from the analysis software show that there are 42 grains in Fig. 13b, while there are 83 grains in Fig. 13c. With all the requisite data for individual grains, grain-related parameters like grain size, grain morphology, grain area, etc., are easily quantified by the analysis engines.

Identification of crystal structure and its orientation also allows the EBSD analysis engine to differentiate between various phases. In some cases, where phase differentiation becomes difficult, another SEM-based technique, viz. energy-dispersive spectroscopy (EDS), is brought to use. EDS is another powerful tool which allows one to get quantitative information about composition of a given material along with its spatial distribution. This technique, combined with EBSD, can provide very accurate identification of various phases present in a given material system. Figure 14 shows EBSD maps for duplex steel, which contain both ferrite and austenite phase. Figure 14a shows the IPF map with grain boundaries, while Fig. 14b shows the

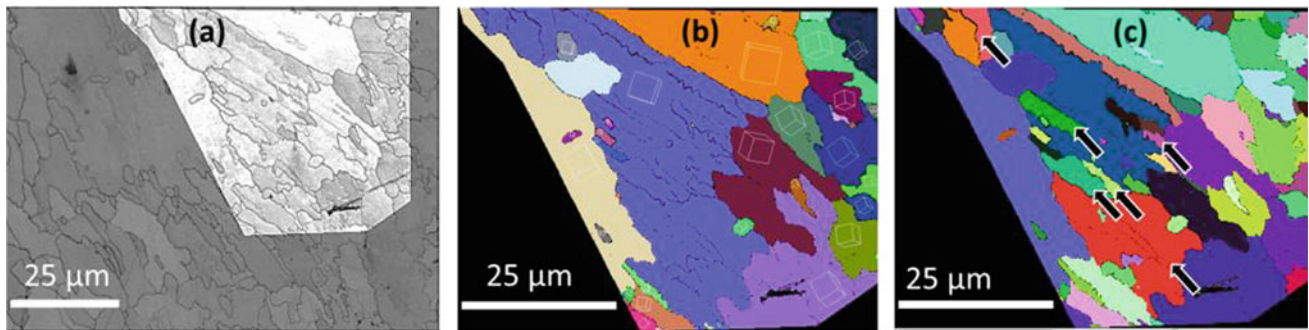


Fig. 13 **a** Region of interest from the original scan is highlighted. **b** Grain map with 10° grain definition. **c** Grain map with 2° grain definition, showing several ‘new’ grains which have been highlighted by arrow

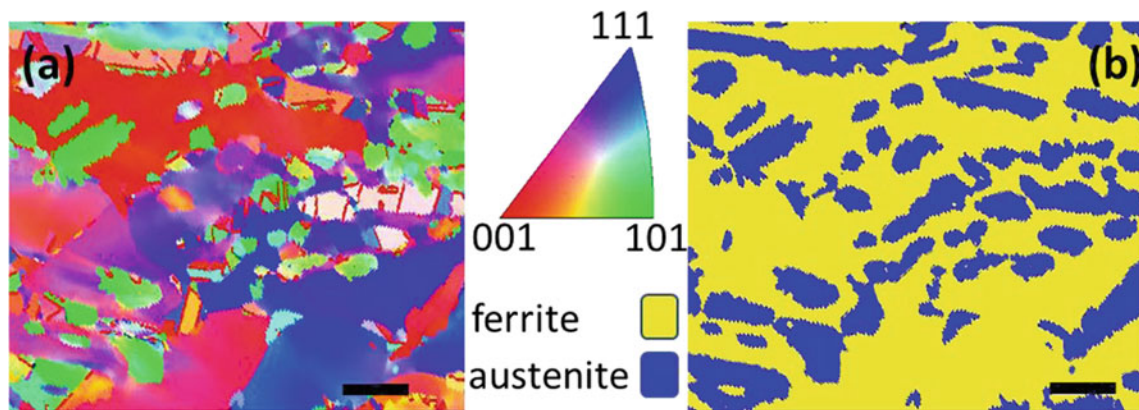


Fig. 14 Duplex steel. **a** Orientation map micrograph based on IPF color (shown here). **b** Corresponding phase map for duplex steel showing austenitic and ferritic phases (scale bar = $100\ \mu\text{m}$)

phase map of the same region, which differentiates between the two phases present in the material. Based on EBSD, it was determined that this material contained 34% austenite and 66% ferrite. This was also confirmed by ferrite scope study of the material.

6.2 Misorientation Analysis

Once we have the orientation information for each and every point or pixel in the scanned area, we can realize that most other microstructural parameters obtained in EBSD are just a derivative of this data. Since orientation is defined by the rotation matrix ‘ g ’, misorientation between two grains inside the same sample whose orientations are defined by rotation matrices ‘ g_1 ’ and ‘ g_2 ’, respectively, can be given by: $M = g_1^{-1}g_2$. Thus, misorientation data for any pair of points or pair of grains can be readily calculated. For data on grain boundaries or phase boundaries, misorientation data only from the neighboring points is considered and assigned as interface between the two points. The matrix form of representation of misorientation is very convenient for

mathematical transformations and calculation, but misorientations are usually represented as axis–angle pair. Axis–angle pair are not unique, and depending on the symmetry of the crystal, one may obtain several sets of these axis–angle pairs. For instance, for cubic symmetry there are 24 symmetrically equivalent orientations, and this leads to $576 (=24 \times 24)$ symmetrically equivalent misorientations. In such cases, the misorientation with the lowest angle is considered as the misorientation angle or also known as disorientation angle.

One of the simplest representations of misorientation data is the misorientation plot, which presents the frequency of occurrence of various misorientation angles between the neighboring grains of a particular microstructure (Randle et al. 2001). Misorientation plot for the Inconel sample is given in Fig. 15a. As stated earlier, misorientation angle is just one aspect of the misorientation data, and for a complete understanding of the interface between grains, one needs to also identify the misorientation axis and the boundary plane. In general, an interface between two grains is defined by five degrees of freedom. Three of these parameters are associated with misorientation and other two with the interface plane.

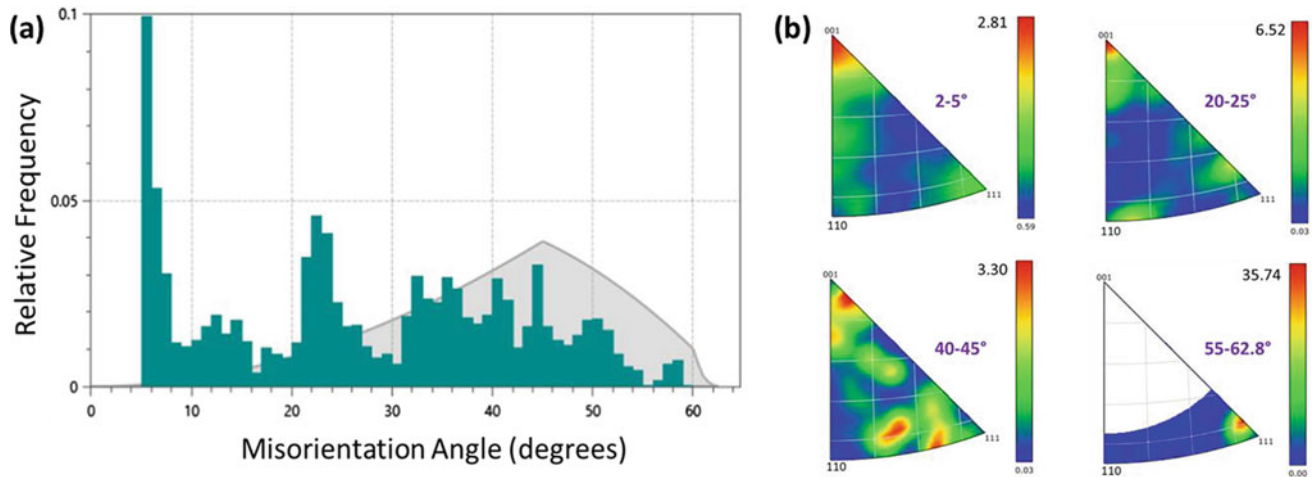


Fig. 15 **a** Misorientation distribution map for Inconel 718 sample. (Gray line indicates theoretical distribution of misorientation for a perfectly random polycrystalline material.) **b** Misorientation axis distribution of the Inconel 718 sample for four different angle ranges

For certain types of boundaries, misorientation angle is not sufficient, and they must be presented in terms of axis–angle pair. A set of axis–angle data obtained from Inconel 600, which is a single-phase material, is presented in Fig. 15b. This data shows the distribution of axis for various angle ranges. Another type of boundary of interest is coincident site lattice (CSL) boundaries, which have certain axis–angle pair that show distinct properties. These boundaries can also be extracted from the orientation and grain data and provide useful information to analyze the microstructure of the material. EBSD has come out as a powerful technique for this field of study, usually called grain boundary engineering. A case study has been provided for appreciation of the utility of EBSD in getting in-depth information about microstructure of material and thereby improving its characteristics.

6.3 Micro-strain Analysis

Residual strain inside the material is an important microstructural parameter that can also be extracted from EBSD data. Plastic strain in the material gets stored as an array of dislocations, which lead to misorientation inside the grain. These misorientations can be calculated in various ways to get different types of information. Some of the most widely used EBSD parameters to represent strain are kernel average misorientation (KAM), grain orientation spread (GOS), and grain reference orientation deviation (GROD). KAM is basically average misorientation of each point with respect to all its neighbors. This parameter is very useful in visualizing localized strains in a sample. Schematic representation of definition of KAM is shown in Fig. 16a.

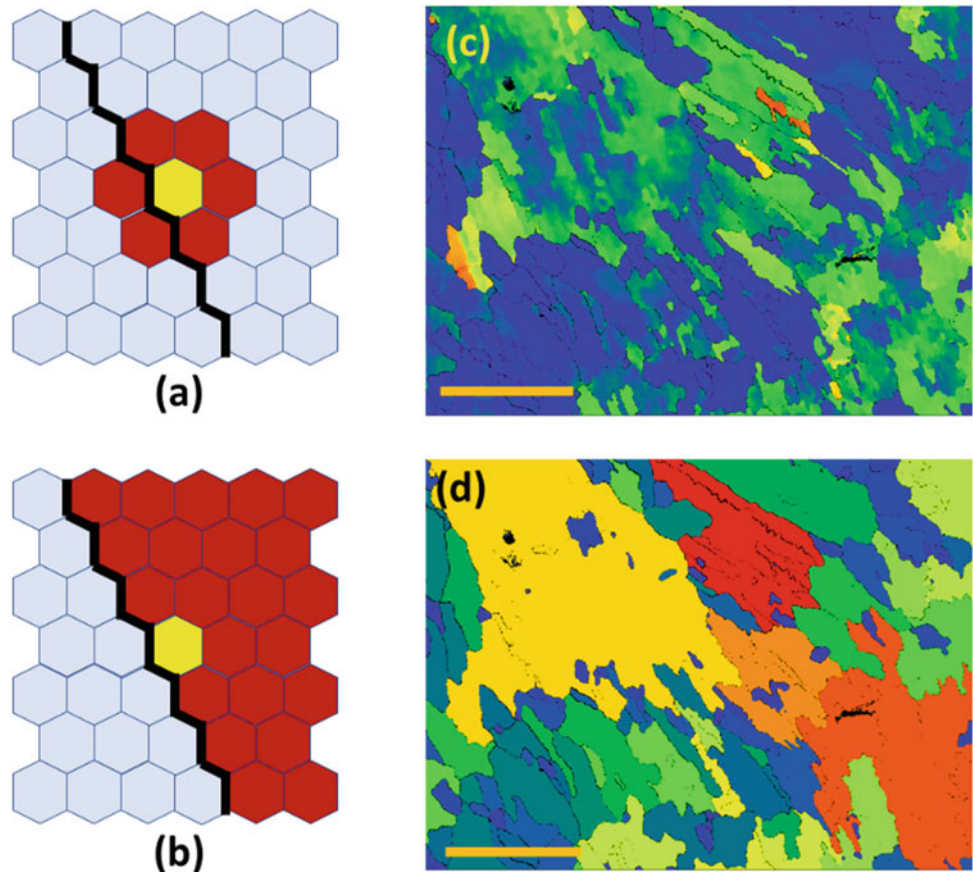
GOS, on the other hand, represents average spread of the orientation of each grain. This is very useful in

understanding average level of strains for individual grains and thus differentiating between the recovered and recrystallized grains from deformed grains. Grains with very low GOS value can be considered as recrystallized grain and free of any strains, while grains with very high GOS value can be considered deformed and still strained. Schematic representation of the definition of GOS and a GOS map for Inconel 718 is shown in Fig. 16b and d, respectively. Another data that is useful in understanding strains inside individual grains is intra-grain misorientation. One way to represent this is by using GROD, where the average misorientation of each point is calculated with respect to the mean orientation of the grain. This is very useful in bringing out the substructures inside a grain. KAM and GROD are similar in character and represent the deviation of individual pixels. The primary difference between the two parameters is that KAM is deviation calculated with respect to immediate neighbor orientations while GROD is deviation calculated with respect to the average orientation of the grain. A GROD map for Inconel 718 is shown in Fig. 16c. Some examples on the use of KAM and GOS to quantify the residual strain present in the material can be found in Sahu et al. 2019; Yadav et al. 2018; Yadav et al. 2019.

6.4 Micro-texture Analysis

We pointed out earlier that a complete understanding of orientation cannot be obtained from the orientation map or any other map for that matter. Maps represent only one parameter of the orientation (e.g., normal direction, Euler angle value, etc.), while orientation has at least three parameters (e.g., three perpendicular orientations or three Euler angles, etc.). It is possible to present the orientation data in three-dimensional space of the Euler angles, and this

Fig. 16 Schematic explanation of the calculation of **a** KAM and **b** GOS. (Each hexagon represents individual point or pixel of EBSD map.) **c** GROD map and **d** GOS map of Inconel 718 sample



is called orientation distribution (OD). OD does not contain any information on spatial distribution of the pixels, and it only provides information related to density of pixels in this three-dimensional space. It is possible to obtain mathematical probability of orientation distribution, and in that case, it is called orientation distribution function (ODF) (Bunge and Haessner 1968; Bunge 2013). OD and ODF have served as powerful tools in texture analysis of materials. Occurrence of high density of crystal orientations in a particular Euler space denotes particular properties or phenomena in the material. A schematic of various texture components found in the cubic system in Euler space is shown in Fig. 17a (Humphreys 2001). Since plotting and analyzing a 3D information is difficult, this 3D space is cut into slices of 5° along the φ_2 -axis. Hence, ODF is a 2D representation of Euler space. Orientation distribution (in 2D) of Inconel 718 sample is presented in Fig. 17b.

Another powerful tool for representation of texture is pole figures and inverse pole figures. Pole figure represents the orientation of a particular crystallographic plane with respect to sample coordinates. It basically shows the alignment of sample coordinates with the crystallographic pole. The term ‘pole’ refers to the normal of a given crystallographic plane intersecting a hemisphere and projected in two-dimensional

plane (see Fig. 18). Pole figures can be generated for any particular crystallographic plane, but are meaningful only for certain low-index planes. Schematic of $\{111\}$ pole figure of a cubic system giving rise to cube texture, copper texture, and brass texture is shown in Fig. 19. Here, RD, ND, and TD refer to the rolling direction, normal direction, and transverse direction, respectively, of the sample coordinate system. It is useful to recall that pole figures represent data with respect to the sample orientation, and hence, symmetry of the sample will also get reflected in the pole figure.

Inverse pole figure (IPF), as the name suggests, is an inverse representation of data. In IPF, all the crystallographic orientations are represented with respect to a particular sample direction (usually ND). Basically, IPF shows the alignment of crystallographic poles with a specified sample direction. Here too, crystal symmetry is reflected in the inverse pole figure. For cubic systems, we know that there are 24 symmetrically equivalent orientations, which are represented as 24 triangles in the stereographic projection (see Fig. 20a). Hence, for cubic crystal systems, representation of only one standard stereographic triangle is sufficient, shown in Fig. 20b. We can add unique colors to the orientations at the three corners of the triangle, leading to a mix of these colors for all other orientations, as shown in

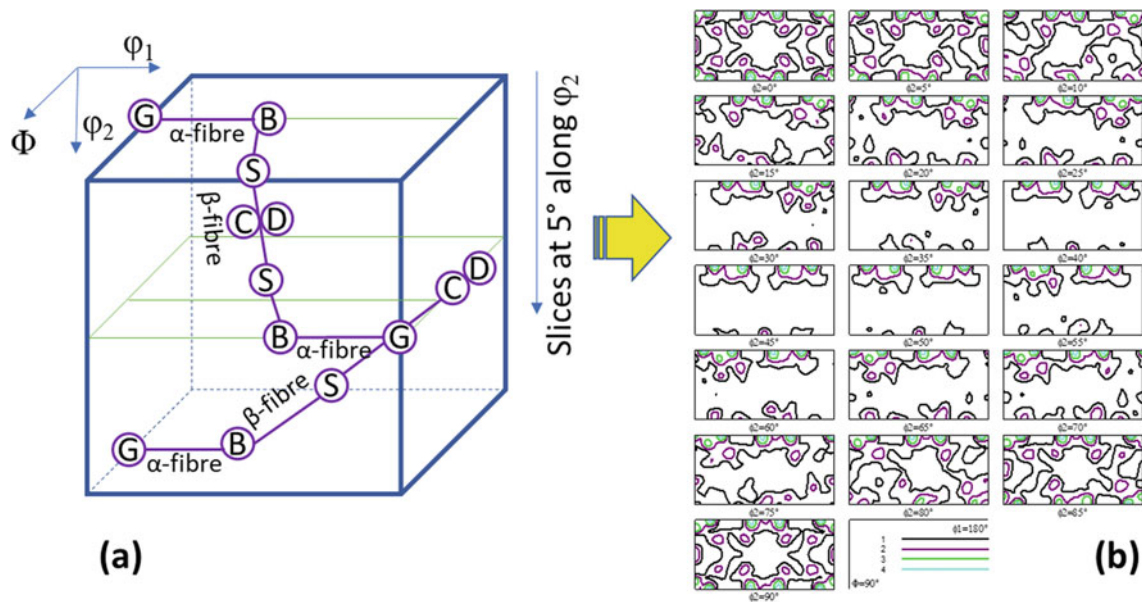


Fig. 17 **a** A schematic of various texture components found in cubic system in Euler space (adapted from ref Humphreys (2001)). **b** ODF map for Inconel 718

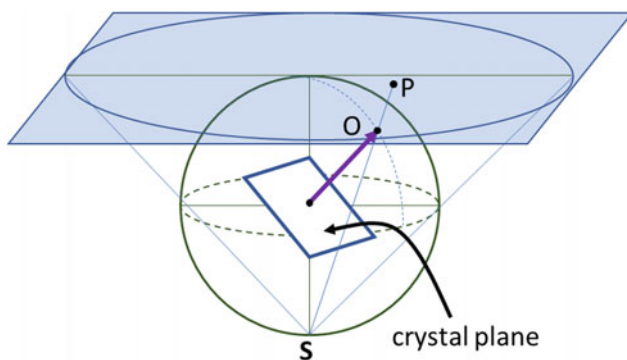


Fig. 18 Origin of pole figure: A crystal plane is shown whose normal intersects with the surface of positive hemisphere at point 'O'. 'S' is the light Source Which when passes through 'O' is projected in 2D plane at 'P', which is called the pole of the crystal plane. Adapted from ref Schwartz et al. 2009

Fig. 20c. This pseudo-colored IPF triangle is utilized for generating the pseudo-colored orientation maps shown earlier for Inconel 718, which has cubic symmetry. For lower symmetry crystal structures, there will be lesser number of the fundamental repeating unit from this stereographic projection, which can be used to add pseudo-color to the orientation map.

7 Case Studies

In the previous section, we gave a brief glimpse of various quantitative analyses that is possible from the data acquired using EBSD-based OIM. In this section, we will showcase some case studies where EBSD analysis is put in application

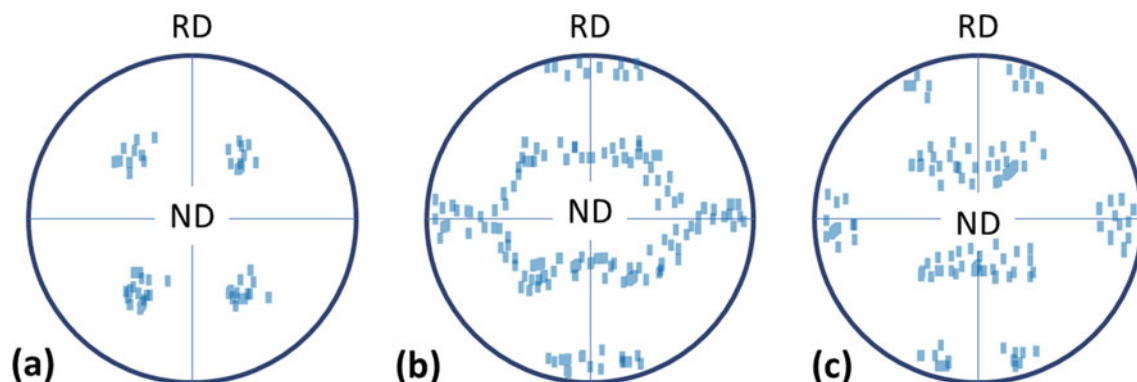


Fig. 19 Schematic of $\{111\}$ pole figure of a cubic system giving rise to **a** cube texture, **b** copper texture, and **c** brass texture. (RD and ND refer to rolling direction and normal direction of the sample coordinate system.). Adapted from ref Schwartz et al. (2009)

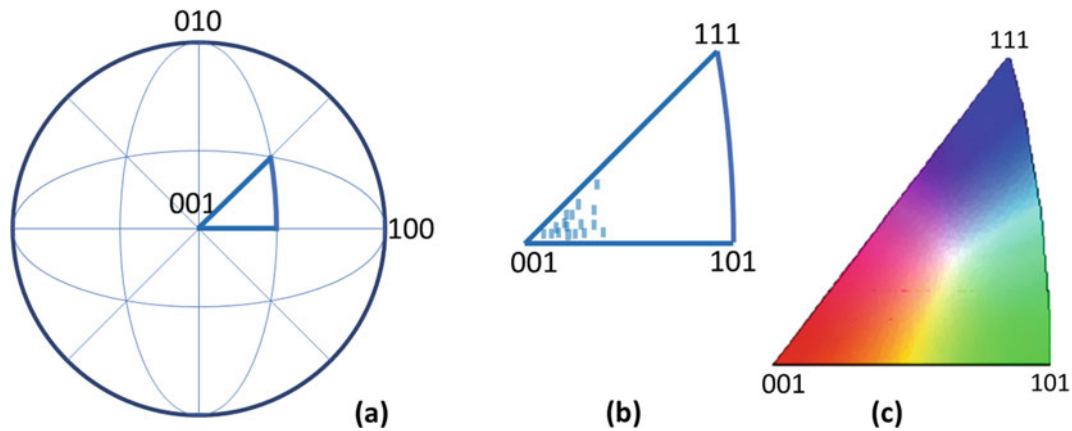


Fig. 20 a Stereo net for the representation of inverse pole figure and the standard stereographic triangle for the cubic system is highlighted. b Schematic of IPF triangle showing the cube texture. c IPF triangle with pseudo-colors which are used for orientation mapping

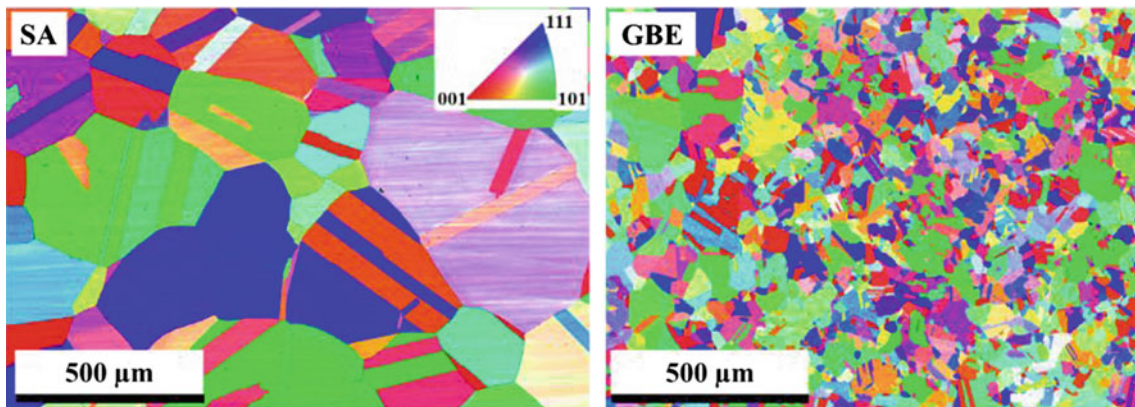


Fig. 21 IPF map of SA and GBE samples

to improve our understanding of the process–structure and structure–property correlation of material.

7.1 Study of Grain Boundary Engineering Using EBSD

EBSD technique is of particular interest, and in fact a necessity, in the field of grain boundary engineering (GBE) (Watanabe 1984; Randle 2004). Specifically, it helps to characterize various interfacial parameters like the fractions of low- Σ coincidence site lattice (CSL) boundaries, grain boundary misorientation deviation, triple junction distribution, and grain boundary connectivity.

The CSL model is used to explain the ‘special’ properties of some high-angle grain boundaries (HAGBs), which are highly resistant against intergranular degradation than random HAGBs. At some particular misorientation relationships, lattices of the two adjoining grains notionally coincide with each other and give rise to another three-dimensional

sub-lattice, known as coincidence site lattice. The degree of coincidence is quantified by a symbol, ‘ Σ ’ (sigma), which indicates the reciprocal of the volume density of coinciding lattice sites, without consideration of the grain boundary plane (Brokman and Balluffi 1981). A deviation in the misorientation angle from the exact coincidence is allowed within which the properties of material do not vary much. The most commonly used criterion for the deviation is Brandon criterion (Brandon 1966), given as $\Delta\theta = \theta_m/\Sigma^{1/2}$ where $\Delta\theta$ is the maximum deviation angle allowed from the exact CSL misorientation and $\theta_m = 15^\circ$. The value of low- Σ CSL is taken for $\Sigma \leq 29$, as $\Sigma > 29$ have only a negligible effect on grain boundary characteristics. $\Sigma 1$ is the same as low-angle grain boundaries. Similar to grain boundaries, triple junctions may also affect intergranular characteristics. Gertsman and Tangri (1995) and Gertsman et al. (1996) classified different types of triple junctions (in 2D) into four kinds, represented as J_i ($i = 0$ to 3), depending upon the number of CSL boundaries they connect. Here, i represents the number of low- Σ CSL boundaries meeting at the triple

junction. Thus, junctions J_2 and J_3 are considered as special/secure junctions for their higher probability to arrest intergranular crack propagation. Junctions J_0 and J_1 are described as non-special/weak junctions for their lower ability in checking the propagation of intergranular degradation. The generation of special triple junctions is also necessary for the effective disruption of the connectivity of random HAGBs networks.

Here, we present a particular case study demonstrating the capabilities of EBSD for the GBE study. In this work, hot rolling and annealing were used as an industrially feasible GBE route to improve the grain boundary structure and, consequently, the functional property (viz. sensitization) of nickel-based superalloy, Alloy 600. Detailed information about this work can be found in Sahu et al. (2019, 2018).

7.1.1 Process–Structure Correlation

EBSD was used to understand the effect of thermomechanical processing on the evolution of microstructure and grain boundary structure. Figure 21 shows the IPF map of solution annealed (SA) and GBE sample conditions. It can be observed that thermomechanical processing leads to a large reduction in grain size by dynamic recrystallization. The variation of colors in the IPF maps in both the conditions indicates that there is no strong texture in either the SA condition or after the processing. The effect of processing on grain boundary structure has been quantified by measuring the fractions of special grain boundaries ($3 \leq \Sigma \leq 29$) and special triple junctions ($J_2 + J_3$), and it is shown in Fig. 22. It can be observed that the thermomechanical processing leads to an increase in not only the fraction of special boundaries but also the fraction of special junctions. In other words, this particular processing condition leads to grain boundary engineering as well as triple junction engineering in Alloy 600. This plot also distinguishes the characteristics of solution annealed and grain boundary engineered sample conditions. Even though $\sim 60\%$ special boundaries in the case of solution annealed sample are a fair fraction, a low fraction of special triple junctions makes it unsuitable to be called as grain boundary engineered condition. To further appreciate this effect, information regarding disruption of HAGBs network with the introduction of twin boundaries was collected with the help of twin-related domain (TRD) analysis (Reed and Kumar 2006; Gertsman 2001; Reed et al. 2004). TRD represents a cluster of grains, which are mutually connected by $\Sigma 3^n$ grain boundaries. Thus, a TRD much larger than the grain size would represent extensive multiple-twinning effects leading to high disruption of HAGBs network. The number of grains per TRD for SA and GBE condition has been shown in Fig. 22. This value is very high (15.9) for GBE sample condition in comparison with that of SA (5). Thus, grain boundary map

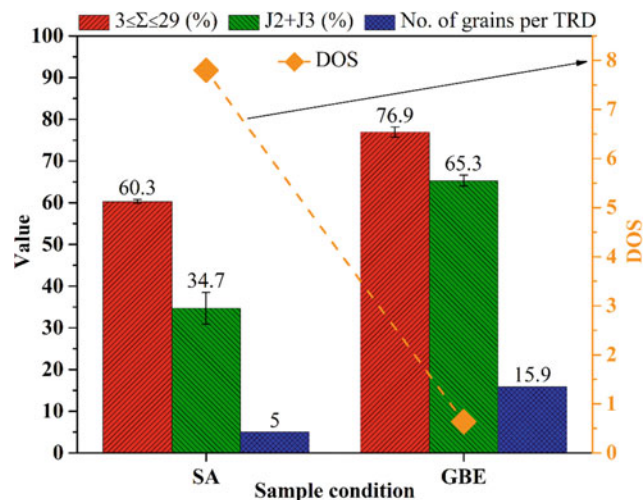


Fig. 22 Effect of thermomechanical processing on the evolution of grain boundary structure and consequently on DOS

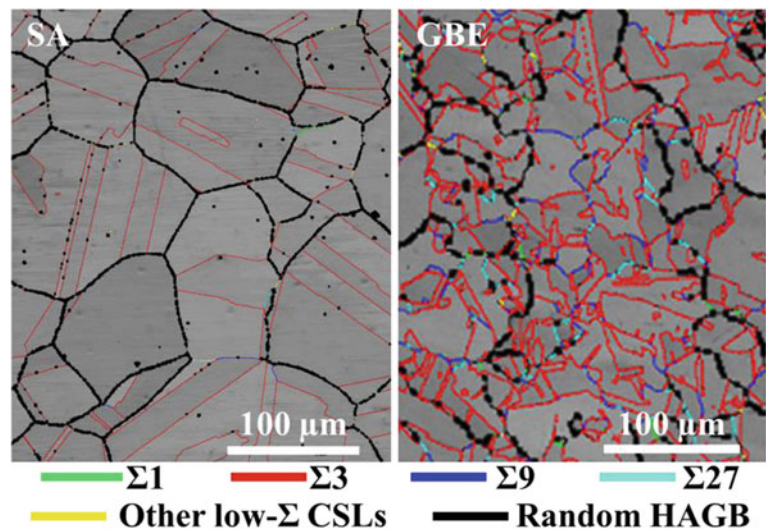
of GBE condition can be expected to show disruption of grain boundaries, while SA condition would show a mutually connected HAGBs network. This is very well reflected in the grain boundary maps of these two particular conditions shown in Fig. 23.

7.1.2 Structure–Properties Correlation

After investigating the effect of thermomechanical processing on grain boundary structure, its correlation with functional property (in terms of sensitization effect) was studied. For it, these two samples were given sensitization heat treatment at 650°C for 24 h, and the sensitization effect was studied with the help of double loop electrochemical potentiometric kinetic reactivation (DLEPR) test (Číhal Vr, Štefec R. 2001). Figure 22 shows the DOS values of the two particular conditions. As expected, a modified grain boundary structure after thermomechanical processing led to a sharp decrease in DOS value for GBE condition in comparison with that of SA sample.

The aforementioned results show an unambiguous correlation between grain boundary structure and sensitization effect; however, the role of individual boundaries on chromium carbide (Cr_{23}C_6) precipitation is not clear from this experiment. In order to analyze the role of individual boundaries, GBE sample was aged at 704°C for various times between 0.5 and 100 h, and then, the precipitation of chromium carbides on individual boundaries was studied using EBSD-based OIM map and scanning electron microscopy (SEM) micrograph (showing the distribution of carbides) in the same regions. A typical subset of the EBSD map showing various kinds of boundaries and the corresponding SEM micrograph showing the precipitation of chromium carbides in 0.5 h aged GBE specimen have been demonstrated in Fig. 24. It can be seen that random HAGBs

Fig. 23 Band contrast map overlaid with grain boundaries showing the effect of thermomechanical processing on the grain boundary connectivity



are very prone to the precipitation of carbides. On the other hand, low deviation $\Sigma 3$ boundaries can be viewed to be void of any carbide precipitation. However, with an increase in misorientation deviation (shown by arrows in Fig. 24), even $\Sigma 3$ boundaries start precipitating chromium carbides. Similarly, $\Sigma 9$ boundaries are observed to have a low density of carbides.

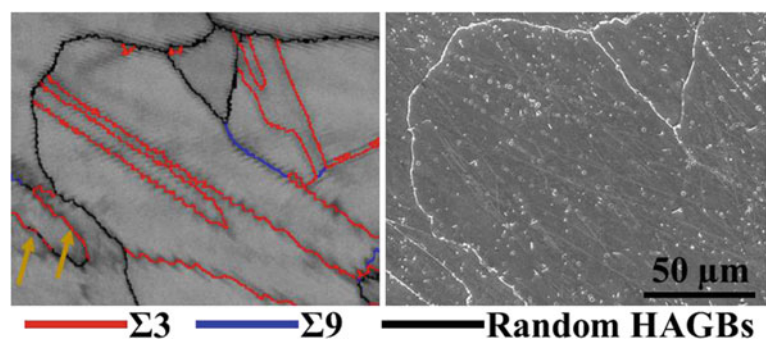
Some more reports on the application of EBSD to study process–structure and structure–property correlation can be found in Yadav et al. 2016, 2018, 2019; Joham et al. 2017; Sharma and Shekhar 2017; Vaid et al. 2016. In conclusion, this case study showcases the capabilities of EBSD as a powerful quantitative characterization tool.

7.2 Study of Geological Materials Using EBSD

Quartz is one of the most common rock-forming silicate minerals, available in a wide range of crustal rocks, and is an important component to determine the rheology and overall dynamics of the crust. The mineral dominantly occurs in granite and granitoids, sandstones and shales, quartzites and schists. Quartz is also exclusively present in quartz veins and

pegmatite dikes. Being a crystalline material, quartz deforms plastically following the laws of dynamic recrystallization under suitable pressure, temperature, and differential stress (Nicolas and Poirier 1976). A typical quartz crystal (right-handed) has several possible slip planes, activation of which is a function of temperature (Fig. 25). The systematic evaluations of such deformation, especially the study of microstructure and texture of the deformed quartz aggregates, provide a series of critical information. This information interprets the ambience, mechanisms, kinematics, and stress magnitude of the overall deformation (Bell and Etheridge 1976; Lloyd and Freeman 1994; Stipp and Tullis 2003; Twiss 1986; Halfpenny et al. 2012; Hunter et al. 2018). Quartz typically deforms maintaining three deformation regimes based on the ambient temperature (Hirth and Tullis 1992)—(i) low temperature (<300 °C); (ii) intermediate temperature (300–600 °C); and (iii) higher temperature (>600 °C). The strain rate is also a crucial factor, which generally decreases at elevated temperatures. Each regime has their characteristic set of microstructures and textures. Optical microscopy with or without universal stage attachment and automated electron backscattered diffraction (EBSD) are two of the most common and popular methods

Fig. 24 (Left) Band contrast map and (right) SE image showing the effect of aging time on carbide precipitation on different kinds of boundaries



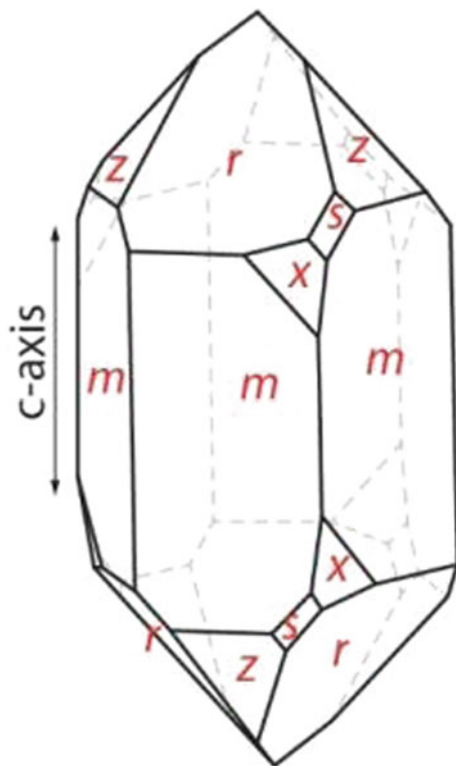


Fig. 25 A typical single quartz crystal (right-handed) showing the different slip planes. The orientation of the *c*-axis is shown by the arrow. The basal plane *a* is orthogonal to the *c*-axis

in order to study the qualitative and quantitative microstructures of quartz.

Here, we present the texture analysis of naturally deformed quartz aggregate. The samples were collected from southern granulite terrain (SGT) in India, and a rock suite underwent metamorphism up to granulite facies (Ghosh et al. 2004). SGT hosts high-grade rocks, like charnockites, khondalites, and other granulite facies metamorphic rocks. The concerned quartz unit typically occurs as discrete stratigraphic unit within the granulites as alternating layers of quartz and iron oxides (magnetite and hematite), popularly referred to as ‘banded hematite quartzite’ and ‘banded magnetite quartzite.’ The ultrahigh temperature and pressure granulite facies metamorphism (1000 ± 50 °C/5–9 kbar) in SGT dates back to 2.5 billion years (Raith et al. 1997; Janardhan 1999), which followed a counterclockwise *PTt* path and exhumation processes due to differential upliftment active in recent geological past.

Observations of the samples under a transmitted light optical microscope reveal that quartz (Qtz) grains are dominantly present as elongated thin micro-bands along with opaque minerals (iron oxides, IOx) and pyroxene (Pyx) grains (Fig. 26a). The quartz grains are dynamically recrystallized; in a few places, triple junctions along the grain boundaries are observed, and a large number of grains show

undulose extinctions (Fig. 26b). Pyroxene grains remain as porphyroclasts and often show weak shear kinematics (Fig. 26a). Polished sections of the samples observed under the scanning electron microscope in backscatter electron (BSE) mode reveal equant shaped iron oxide grains occurring together in the stretched oxide segments (Fig. 26c).

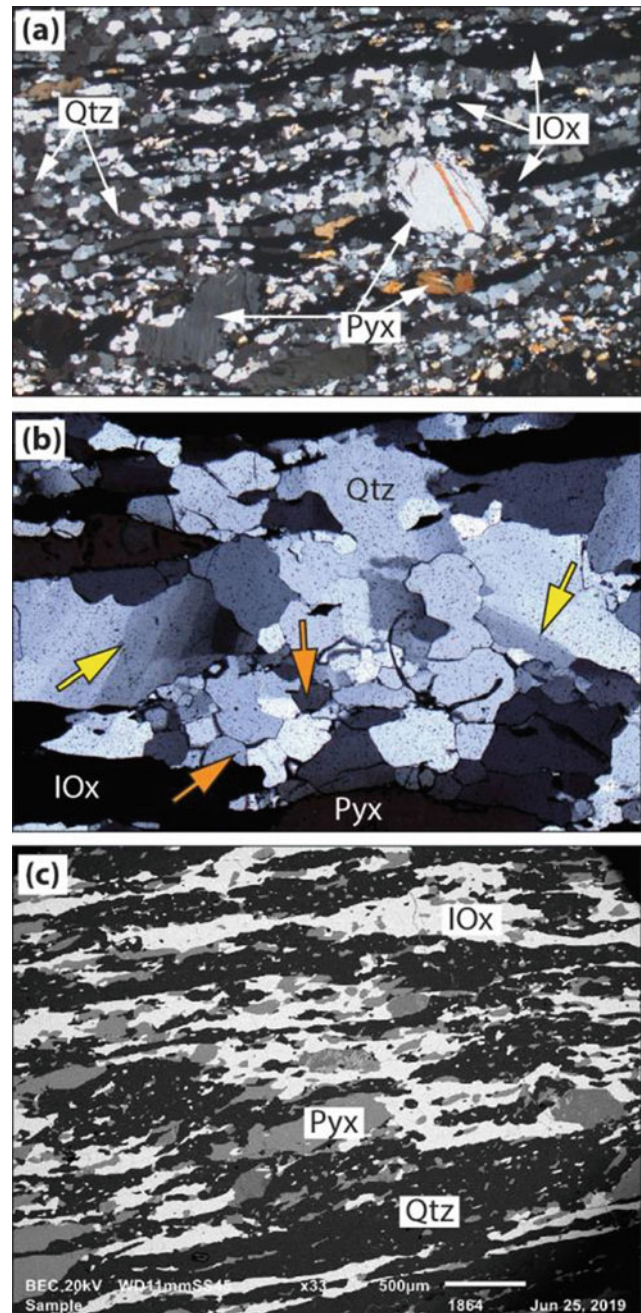


Fig. 26 Transmitted optical (a, b) and backscatter SEM images of the studied samples observed on the XZ plane of the bulk strain ellipse. In (b), the yellow and orange arrowheads point undulose extinctions and triple junctions, respectively, in the quartz grains. Qtz: Quartz; IOx: iron oxides; Pyx: pyroxene. The width of plates a and b is 10 and 2 mm, respectively

We performed EBSD analysis to study the texture of the quartz grains. A representative sample was cut along the XZ section of the bulk strain ellipsoid and prepared for the analysis following the standard protocols of the EBSD polishing. The EBSD analysis was performed using a field emission scanning electron microscope (JSM 7100F) equipped with an EBSD detector (Oxford Instrument NanoAnalysis, UK) keeping the scan surface of the samples tilted at 70°. The EBSD patterns were collected with 20 mm working distance, 2–5 μm step size, 20 kV accelerating voltage, and ~ 13 nA beam current. Data acquisition from the sample and crystallographic patterns were indexed automatically by Aztec Software (Oxford Instrument NanoAnalysis, UK). MTEX (Mainprice et al. 2011), an open-source MATLAB toolbox (version 5.1.1), was employed to post-process data. Data points with confidence index < 0.1 were removed using the software package. The critical misorientation angle to reconstruct individual quartz grains was chosen to be 10°. The data of the quartz grains is presented in phase map, grain orientation spread (GOS) map, kernel average misorientation (KAM) map, inverse pole figure (IPF) map, and pole figures.

We present the results of EBSD analysis in Fig. 27. The phase map shows that the quartz grains dominate the area with a few smaller hematite and magnetite grains (Fig. 27a). The GOS is noted to be within 5° (Fig. 27b). The IPF map reveals the fact that quartz grains are deformed, and in few, they also show sub-grain boundaries (Fig. 27c). The KAM for majority of the grains lies within 0.004, with few grains characterized by thin bands of high values (>0.016 , Fig. 27d). One-point-per-grain pole figures (Fig. 27e–h) are calculated and presented using de la ValléePousin kernel and half width of 15°. The pole figures are contoured to multiples of uniform density (m.u.d). The $\langle c \rangle$ -axis pole figure exhibits a well-defined central girdle. Its obliquity to the XY plane indicates top-to-left sense of shear (Fig. 27e). The cylindricity index (Larson 2018) was calculated to be 0.9, indicating that the quartz grains are highly strained/deformed. Moreover, the maxima of the $\langle c \rangle$ -axis pole figure suggests both rhomb- $\langle a \rangle$ and prism- $\langle a \rangle$ planes were dominantly active, implying deformation within 400–500 °C (Passchier and Trouw 2005). The location of the maxima of the $\langle a \rangle$ -axis pole figure (Fig. 27f) also confirms the same.

7.3 Study of the Effect of Machining Parameters on Subsurface Deformation Using EBSD

Machining is known to make structural changes to not only the surface, but also the subsurface of a machined component (Abolghasem et al. 2012; Shekhar et al. 2012; Wang et al. 2017). The strain, strain rate, and associated

temperature rise and eventual microstructural changes in the chip and surface depend largely on the machining configuration. This microstructural transformation leads to change in the functional (Majumdar et al. 2015; Prakash et al. 2015a, b) as well as the mechanical response of the machined component (Gidla 2017; Verma 2014). Surface characteristics like roughness and hardness are known to have an impact on material failure that initiate from the surface such as fatigue failure, fretting fatigue, wear, and stress corrosion cracking as the surface is in contact with the environment (Yuri et al. 2003; Al-Samarai et al. 2012). The surface characteristics of a machined component are also resultant of the machining conditions used during the final shaping operation of the component. Thus, machining parameters affect the surface characteristics as well as the subsurface microstructure of the finished components, which in turn play an important role in deciding the mechanical and functional response of the material.

The overarching goal of this study was to optimize the machining parameters to improve surface characteristics and improve material performance. The specific objective of this work was to understand the effect of machining parameters on the subsurface microstructure and correlate it with surface characteristics. In this regard, simple orthogonal machining of SS316L using tungsten carbide tool was performed on CNC machine. We selected wear volume and hardness as our measure of surface characteristics and microstructure was characterized using EBSD technique. Steel rod was machined at two different speeds (30 and 180 mm/min) for two different feeds (0.05 and 0.2 mm/rev) at two different depths of cut (DOC) (0.1 and 0.5 mm) keeping tool parameters constant, i.e., rake angle (zero degree) and nose radius (0.4). 8-mm disks were taken from the rod, and overall, we had 8 sample conditions as listed in Table 1. Each of these samples was characterized for roughness using optical profilometry. Ball on disk method was used to conduct tribological studies. Tungsten carbide ball has 6-mm diameter, and the sample was made as the disk having diameter 55 mm and thickness 8 mm.

EBSD technique was utilized for characterizing the subsurface microstructure of the machined surface. Small samples from close to the machined surface were taken, and rectangular scans were taken on the transverse region from near the surface toward the inside of the sample. Orientation maps (overlaid on band contrast map and grain boundary map, shown in black) from an area of 120 $\mu\text{m} \times 40 \mu\text{m}$ for various sample conditions are presented in Fig. 28. The machined surface is shown by the direction of the arrow. Most of the samples show severe deformation near the surface. The black dots near the surface represent the un-indexed points, which point to some strain in the matrix. The extent of depth of these black dots indicates the extent of subsurface deformation. In some of the conditions, one

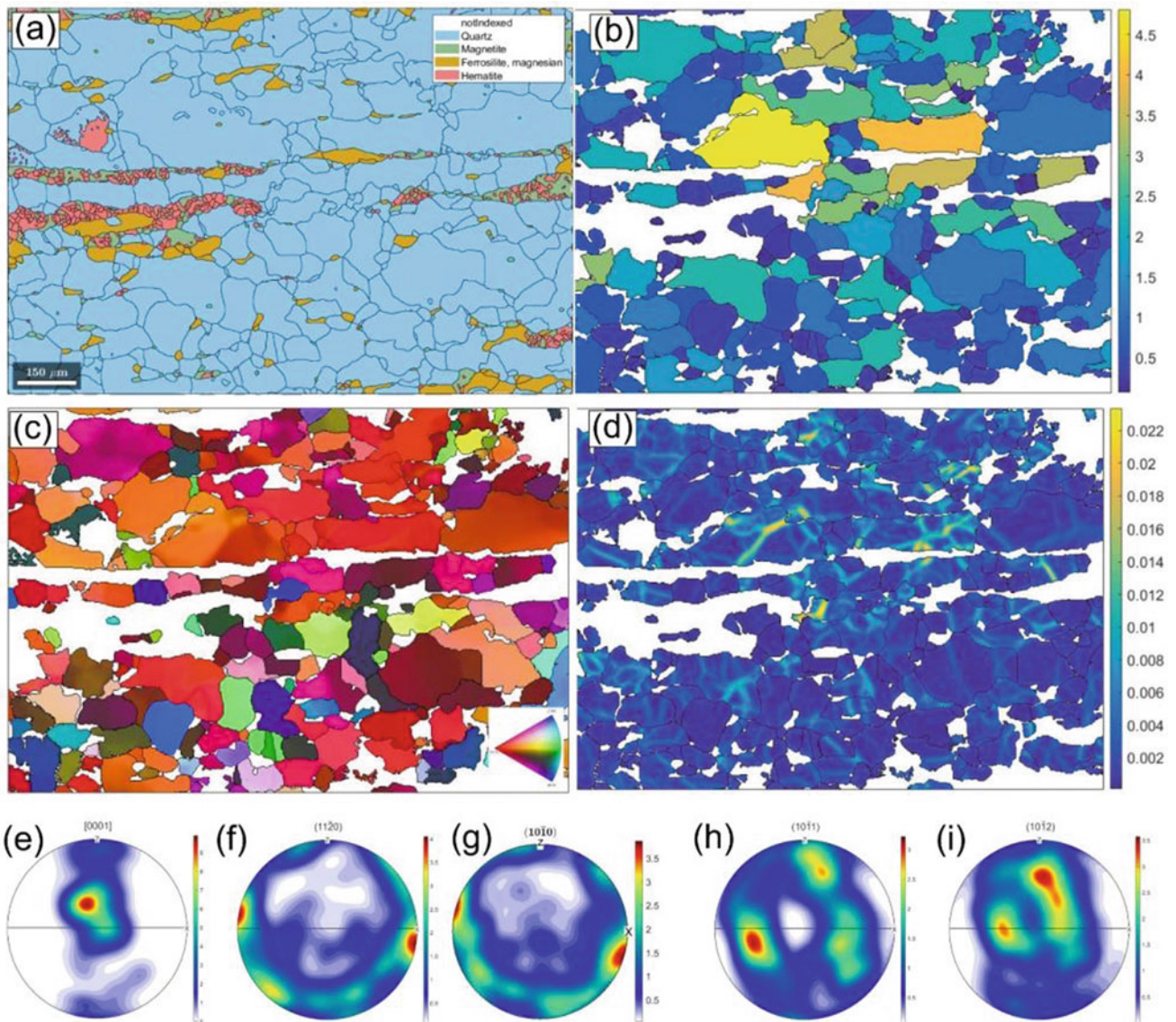


Fig. 27 Selected results of the EBSD analysis. **a** Phase map, **b** grain orientation spread (GOS) map, **c** inverse pole figure (IPF) map along with the key at the inset, **d** kernel average misorientation

(KAM) map. One-point-per-grain pole figures of **e** $\langle c \rangle$ -axes, **f** $\langle a \rangle$ -axes, **g** $\{m\}$ -planes, **h** $\{r\}$ -planes, and **i** $\{z\}$ -planes of the quartz grains. The scale is shown only for **a** so as to avoid repetition

Table 1 Details of machining parameters that were selected for machining of SS316L

Sample	Speed (mm/min)	Feed (mm/rev)	Depth of cut (mm)	Rake angle	Nose radius
S1F1D1	30	0.05	0.1	0	0.4
S1F1D2	30	0.05	0.5	0	0.4
S1F2D1	30	0.2	0.1	0	0.4
S1F2D2	30	0.2	0.5	0	0.4
S2F1D1	180	0.05	0.1	0	0.4
S2F1D2	180	0.05	0.5	0	0.4
S2F2D1	180	0.2	0.1	0	0.4
S2F2D2	180	0.2	0.5	0	0.4

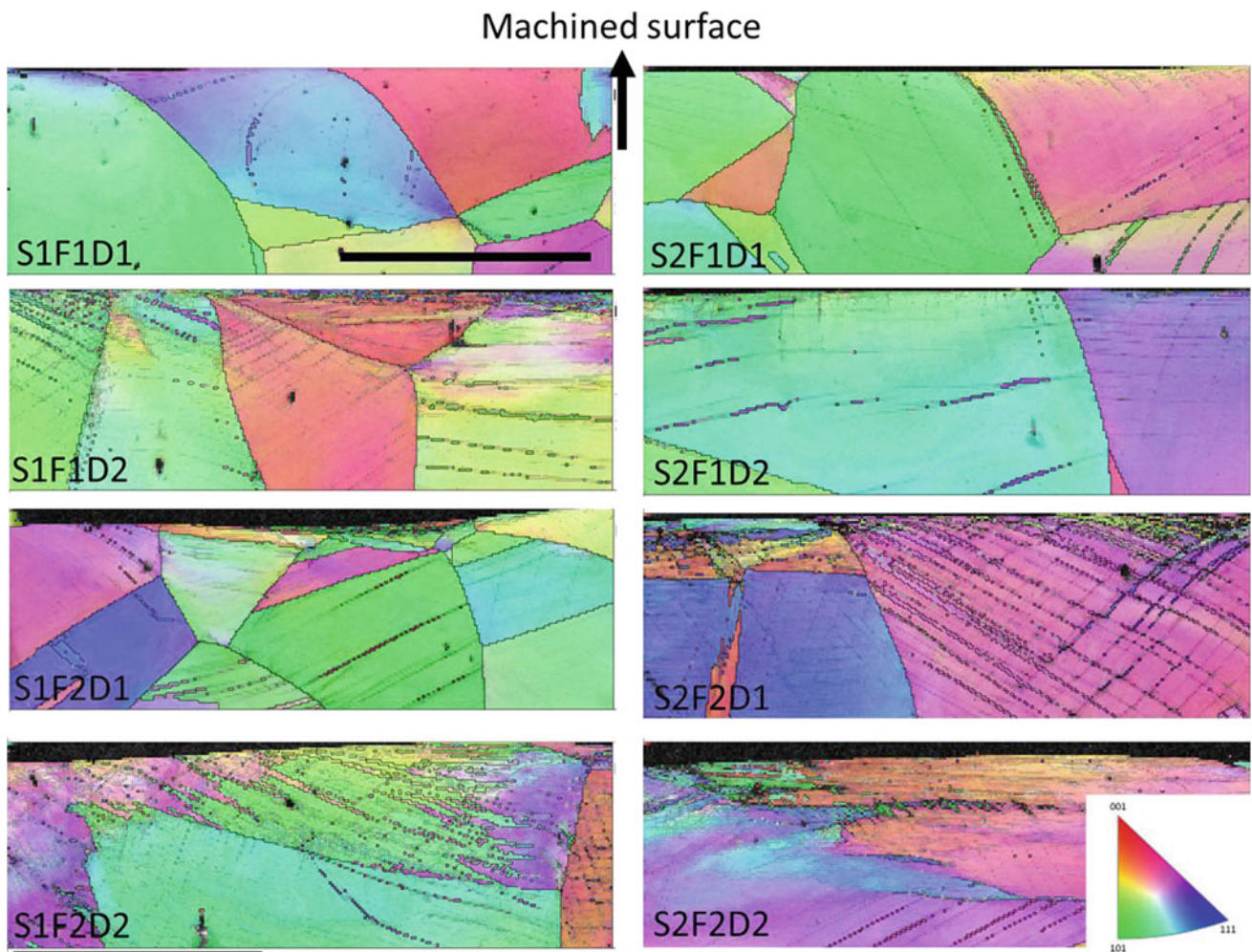


Fig. 28 Orientation maps (overlaid with band contrast map and grain boundary map shown in black) for samples machined under various conditions (scale bar = 50 μm ; same for all micrographs)

can see some very refined grains very close to the surface, but it is not there in most of the other conditions. One can conclude that grain refinement, if it happened, was limited to few micrometers near the surface. However, the subsurface deformation does extend much below this. In order to get a better understanding of the subsurface deformation, GROD maps were generated from the EBSD data.

Roughness values and wear volume were plotted for various sample conditions along with the corresponding GROD map in Fig. 29. Here, one can very easily find a correlation between the smaller subsurface deformation and good (low values) roughness condition on the surface (S1F1D1 and S2F1D1). It is likely that subsurface deformation leads to massive slips on various planes, which leads to poor roughness (S1F1D2, S1F2D2, and S2F2D2). On the other hand, best wear resistance is obtained when we have very large subsurface deformation (S1F2D2 and S2F1D2). It is expected as subsurface deformation results in higher

hardness near the surface, yielding better wear resistance. However, we found that some sample conditions yield good surface roughness as well as good wear resistance (S2F1D1 and S2F1D2). This most likely happens when there exists a very thin layer of subsurface deformation. A thin layer of subsurface deformation results in minimal upheaval on the surface while still resulting in high hardness for good wear resistance. A closer look at the data also suggests that roughness improves with an increase in speed, decrease in feed, and DOC.

This study clearly establishes that EBSD technique can provide a wealth of information about microstructure. In this work, we were able to relate the surface characteristics to the machining parameters and, in turn, to the subsurface microstructure. This improves our understanding in optimizing the machining parameters to obtain better microstructure as well as better surface characteristics.

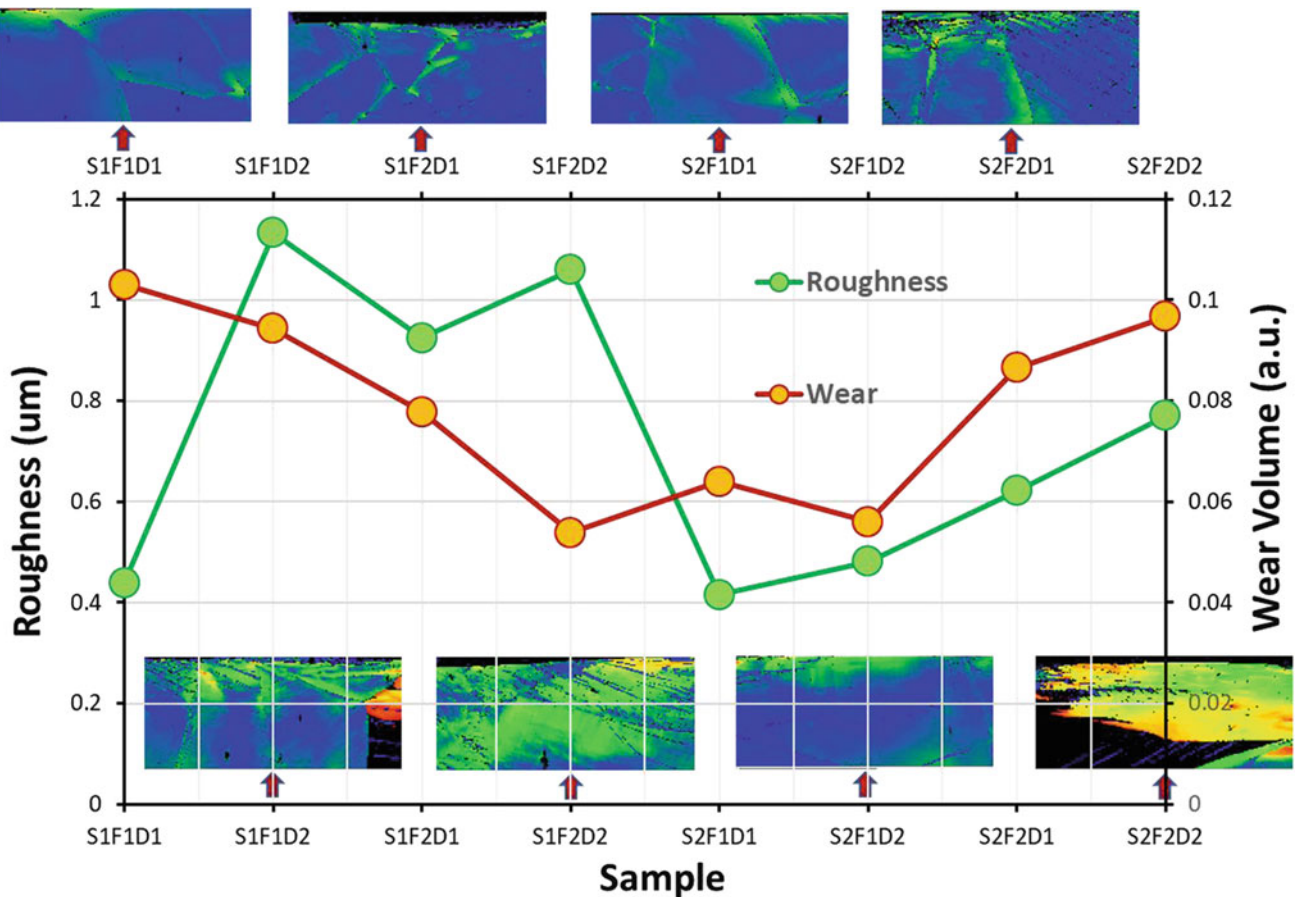


Fig. 29 Variation of roughness and wear volume for various sample conditions (machined surface is toward the top side of each micrograph)

8 Accuracy and Limitations of EBSD

The accuracy with which an absolute orientation of a crystallite can be measured using EBSD is typically $\sim 1^\circ$ (Humphreys 2001; Schwartz et al. 2009; Humphreys and Brough 1999). This value is dependent on the EBSD acquisition parameters, calibration of the EBSD system, and sample alignment conditions. Although the accuracy of the measurement of an orientation is an important factor in determining the usefulness of EBSD, applications of EBSD in the characterization of grain boundaries and their correlation with properties require very accurate measurement of the relative orientation between the neighboring pixels (Humphreys 2001; Humphreys et al. 1999). Accuracy in the relative orientation becomes even more critical in the case of low-angle grain boundaries, especially the interfaces between sub-grains in the deformed samples (Humphreys et al. 1999; Prior 1999; Wilson and Spanos 2001). Since this relative orientation, or misorientation, is calculated using the absolute orientation data, the accuracy of the measurement of misorientation is related to the precision with which the

absolute orientation of individual crystallites can be obtained.

Ideally, all the absolute orientations within a same crystallite should be same, and there should not be any scatter in the orientation data. However, due to the inherent limitations of EBSD, there is a definite value of this orientation noise, ranging from 0.5 to 1° (Wilkinson 2001). These limitations include various factors such as accuracy of pattern solving using Hough transform, CCD camera settings, detector calibrations, accuracy of band detection, and sample alignment. This orientation noise also creates a scatter in the measured data of misorientation between the individual orientations. While this scatter in misorientation data is relatively smaller ($\sim 0.2^\circ$ for misorientation angles higher than 2°) for higher angle grain boundaries, scatters even higher than the actual misorientation for low-angle grain boundaries make an accurate determination of small misorientation angles very difficult (Wilkinson 2001). This further inhibits the study of finer details of a microstructure using misorientation-based parameters like grain average misorientation (GAM), grain orientation spread (GOS), and kernel average misorientation (KAM). Similar to misorientation angles, accurate

Table 2 Typical angular resolution of EBSD in the form of scatter in the measured orientation data (Wilkinson 2001)

Scatter type	Average scatter	Maximum scatter
Absolute orientation	0.5°	1.4°

determination of the misorientation axis also poses certain challenges and is also dependent on the noise of absolute orientation data. Scatter in misorientation axis is not significant for higher misorientation angles. However, the measured misorientation axis for low misorientation angles (<5°) can cover almost complete inverse pole figure, hence making the accurate determination practically impossible (Wilkinson 2001).

Tables 2 and 3 provide a summary of the values of the scatter in the measured orientation and misorientation data, respectively. Average and maximum scatters in the measured orientation data are 0.5 and 1.4°. This scatter is a result of the low precision in the measurement of an individual orientation. As discussed earlier, this precision in the measurement of absolute crystal orientation becomes a limiting factor in the estimation of relative crystal orientation and hence in the characterization of very low-angle grain boundaries. It also makes the application of conventional EBSD potentially inadequate for the characterization of microstructures having deformation features.

Misorientation data is tabulated for 3 different actual misorientation angles, viz. 20, 2, and 0.2°. Maximum scatter in the data of misorientation angles is the standard deviation of the data for each case. It can be seen that for very small misorientation angles such as 0.2°, the scatter in misorientation angle is 0.4°, which is even higher than the actual misorientation angle, and hence, the accurate determination of small misorientation angle is very difficult. In the case of misorientation axis, angles between the measured misorientation axis and the actual misorientation axis are first calculated. Mean scatter and maximum scatter for the misorientation axis are then the mean and maximum value of this data set. Maximum scatter in the misorientation axis for

very small misorientation angles reaches such a high value that it becomes practically indefinite, hence written as ‘indefinite’ in the table.

Improvement in the overall angular resolution of the EBSD technique requires the minimization of the scatter in misorientation data generated. This can ensure the routine and more reliable characterization of very small misorientation angles (<2°). One of the ways to minimize the scatter is either by statistically averaging the orientation data (Humphreys 2001; Wright et al. 2015) or by subtracting a Gaussian-type noise function (Humphreys 1999; Sharma and Shekhar 2018). Although this approach can lead to an improvement in misorientation angle distribution at smaller misorientation angles, improvement in the individual misorientation is not achieved. Changing the operating conditions such as probe current to enhance the quality of backscattered patterns is yet another way to improve the angular resolution (Humphreys and Brough 1999). However, this approach would lead to a decrease in the pattern collection speed and hence will be limited for very smaller area maps. Another approach is to improve the fundamental pattern detection, matching, and solving techniques, including cross-correlation (Bate et al. 2005; Brough et al. 2006; El-Dasher et al. 2003; Wright et al. 2017). These methods are essentially based on the recording of small changes in the absolute positions of similar features in the two patterns from adjacent pixels.

Since this method improves the angular resolution significantly, the EBSD technique with the improved pattern solving method is also known as high-resolution electron backscatter diffraction (HR-EBSD) (Schwartz et al. 2009). Table 4 shows the typical scatter values obtained using a routine HR-EBSD technique. It can be seen that maximum scatter in misorientation angle is only 0.02° even for misorientation angles as small as 0.2°. Maximum scatter in the misorientation axis is also lowered to a definite value of ~14°. This data shows that the EBSD technique with these improved pattern-solving capabilities can be confidently utilized for the routine characterization of deformation

Table 3 Typical angular resolution of EBSD in the form of scatter in the measured misorientation data (Wilkinson 2001)

Actual misorientation	20°	2°	0.2°
Misorientation angle (maximum scatter)	0.2°	0.25°	0.4°
Misorientation axis (mean scatter)	2°	15°	50°
Misorientation axis (maximum scatter)	5°	40°	-Indefinite-

Table 4 Typical angular resolution of HR-EBSD in the form of scatter in the measured misorientation data (Wilkinson 2001)

Actual misorientation	0.2°
Misorientation angle (maximum scatter)	0.02°
Misorientation axis (mean scatter)	5.7°
Misorientation axis (maximum scatter)	13.9°

constituents. This way, the HR-EBSD technique has proved to be pathbreaking in the characterization of localized strains with high resolution (Wilkinson et al. 2014).

It should also be noted that these methods are quite resource-intensive and require a lot of computer space for storing all the electron backscatter pattern (EBSP) data and, in turn, resulting in the increased cost for overall EBSD characterization. However, such limitations are gradually waning with the improvement in computing and storage capabilities.

9 Summary

It is clearly established that EBSD is a very powerful technique that can be applied to all types of crystallographic materials, ranging from metals to ceramics to semiconductors. We provided fundamentals on the origin of Kikuchi pattern and how this data is acquired by the hardware to identifying the orientation of a given material. We have also provided a glimpse of various fundamental analyses that can be carried out with the data extracted using EBSD. Analysis of the data can provide various in-depth understandings of the microstructure and its properties, and this was clearly brought out with the help of some of the case studies discussed here. Toward the latter part, we have also discussed the limitations of this instrument, particularly in terms of the accuracy of the data obtained. This must be kept in mind when interpreting the results and deriving conclusions. It should also be noted that there are several journal articles and books available on the topics listed above, which discuss at length each of these issues. The purpose of this article is to provide the beginners all the necessary information at one place, without getting distracted by great many details. Readers who are looking to gain an in-depth understanding of the subject are directed to the references cited in this article.

Acknowledgements All the EBSD data was generated using the facilities in the Advanced Centre for Material Sciences (ACMS) of IIT Kanpur. Mr. Sivakumar assisted in EBSD data acquisition for the Inconel 718 sample. EBSD of duplex steel was acquired by Prince Setia. Saquib Abdullah, Dripta Dutta, and R. Sarvesha assisted in the EBSD data acquisition and analysis of quartz in case study (B). A part of the work in case study (B) is supported by a DST Swarnajayanti Fellowship (DST/SJF/E&ASA-01/2015-16), awarded to Santanu Misra. Case study (C) is part of the project funded by BRNS, under sanction No. 36(2)/14/39/2016-BRNS/6047.

References

- Abolghasem S, Basu S, Shekhar S, Cai J, Shankar M (2012) Mapping subgrain sizes resulting from severe simple shear deformation. *Acta Mater* 60(1):376–386
- Ahmed J, Wilkinson AJ, Roberts SG (1997) Characterizing dislocation structures in bulk fatigued copper single crystals using electron channelling contrast imaging (ECCI). *Philos Mag Lett* 76(4):237–246
- Al-Samarai RA, Haftirman KRA, Al-Douri Y (2012) The influence of roughness on the wear and friction coefficient under dry and lubricated sliding. *Int J Sci Eng Res* 3(4):1–6
- Bate PS, Knutsen RD, Brough I, Humphreys FJ (2005) The characterization of low-angle boundaries by EBSD. *J Microsc* 220(1):36–46
- Bell TH, Etheridge MA (1976) The deformation and recrystallization of quartz in a mylonite zone. *Cent Aust Tectonophysics* 32(3):235–267
- Berger D, Niedrig H (1999) Complete angular distribution of electrons backscattered from tilted multicomponent specimens. *Scanning* 21(3):187–190
- Brandon D (1966) The structure of high-angle grain boundaries. *Acta Metall* 14(11):1479–1484
- Brokman A, Balluffi RW (1981) Coincidence lattice model for the structure and energy of grain boundaries. *Acta Metall* 29(10):1703–1719
- Brough I, Bate PS, Humphreys FJ (2006) Optimising the angular resolution of EBSD. *Mater Sci Technol* 22(11):1279–1286
- Bunge HJ, Haessner F (1968) Three-dimensional orientation distribution function of crystals in cold-rolled copper. *J Appl Phys* 39(12):5503–5514
- Bunge HJ (2013) *Texture analysis in materials science: mathematical methods*. Elsevier
- Chen D, Kuo J-C, Wu W-T (2011) Effect of microscopic parameters on EBSD spatial resolution. *Ultramicroscopy* 111(9):1488–1494
- Čihal Vr, Štefec R (2001) On the development of the electrochemical potentiokinetic method. *Electrochimica Acta* 46(24):3867–3877
- Coates DG (1967) Kikuchi-like reflection patterns obtained with the scanning electron microscope. *Philos Mag: J Theor Exp Appl Phys* 16(144):1179–1184
- Dingley DJ, Wright SI, Nowell MM (2005) Dynamic background correction of electron backscatter diffraction patterns. *Microsc Microanal* 11(S02):528–529
- El-Dasher BS, Adams BL, Rollett AD (2003) Viewpoint: experimental recovery of geometrically necessary dislocation density in polycrystals. *Scripta Mater* 48(2):141–145
- Gertsman V (2001) Coincidence site lattice theory of multicrystalline ensembles. *Acta Crystallogr A* 57(6):649–655
- Gertsman VY, Janecek M, Tangri K (1996) Grain boundary ensembles in polycrystals. *Acta Mater* 44(7):2869–2882
- Gertsman VY, Tangri K (1995) Computer simulation study of grain boundary and triple junction distributions in microstructures formed by multiple twinning. *Acta Metall Mater* 43(6):2317–2324
- Ghosh JG, de Wit MJ, Zartman RE (2004) Age and tectonic evolution of Neoproterozoic ductile shear zones in the Southern Granulite Terrain of India, with implications for Gondwana studies. *Tectonics* 23(3):TC3006
- Gidla MR (2017) Effect of machining on mechanical, tribological and functional properties of mild steel, M.Tech. thesis at IIT Kanpur
- Halfpenny A, Prior DJ, Wheeler J (2012) Electron backscatter diffraction analysis to determine the mechanisms that operated during dynamic recrystallisation of quartz-rich rocks. *J Struct Geol* 36:2–15
- Heinz A, Neumann P (1991) Representation of orientation and disorientation data for cubic, hexagonal, tetragonal and orthorhombic crystals. *Acta Crystallogr A* 47(6):780–789
- Herter T, Lott K (1993) Algorithms for decomposing 3-D orthogonal matrices into primitive rotations. *Comput Graph* 17(5):517–527
- Hirth G, Tullis J (1992) Dislocation creep regimes in quartz aggregates. *J Struct Geol* 14(2):145–159

- Humphreys FJ (1999) Quantitative metallography by electron backscattered diffraction. *J Microsc* 195(3):170–185
- Humphreys FJ (2001) Review grain and subgrain characterisation by electron backscatter diffraction. *J Mater Sci* 36(16):3833–3854
- Humphreys FJ, Brough I (1999) High resolution electron backscatter diffraction with a field emission gun scanning electron microscope. *J Microsc* 195(Pt 1):6–9
- Humphreys FJ, Huang Y, Brough I, Harris C (1999) Electron backscatter diffraction of grain and subgrain structures—resolution considerations. *J Microsc* 195(3):212–216
- Hunter NJR, Weinberg RF, Wilson CJL, Luzin V, Misra S (2018) Microscopic anatomy of a “hot-on-cold” shear zone: insights from quartzites of the Main Central Thrust in the Alaknanda region (Garhwal Himalaya). *GSA Bull* 130(9–10):1519–1539
- Janardhan AS (1999) Southern granulite terrain, south of the palghat-cauvery shear zone: implications for India-madagascar connection. *Gondwana Res* 2(3):463–469
- Joham R, Sharma NK, Mondal K, Shekhar S (2017) Low temperature cross-rolling to modify grain boundary character distribution and its effect on sensitization of SS304. *J Mater Process Technol* 240:324–331
- Joy DC, Newbury DE, Davidson DL (1982) Electron channeling patterns in the scanning electron microscope. *J Appl Phys* 53(8):R81–R122
- Kamaladasa R, Picard Y (2010) Basic principles and application of electron channeling in a scanning electron microscope for dislocation analysis. *Microsc: Sci Technol Appl Educ* 3:1583–1590
- Kunze K, Wright SI, Adams BL, Dingley DJ (1993) Advances in automatic EBSP single orientation measurements. *Textures Microstruct* 20:589659
- Larson KP (2018) Refining the structural framework of the Khimti Khola region, east-central Nepal Himalaya, using quartz textures and c-axis fabrics. *J Struct Geol* 107:142–152
- Lloyd GE, Freeman B (1994) Dynamic recrystallization of quartz under greenschist conditions. *J Struct Geol* 16(6):867–881
- Mainprice D, Hielscher R, Schaeben H (2011) Calculating anisotropic physical properties from texture data using the MTEX open-source package. *Geolog Soc, London, Spec Publ* 360(1):175–192
- Majumdar P, Shekhar S, Mondal K (2015) Effect of machining parameters on oxidation behavior of mild steel. *J Mater Eng Perform* 24(1):484–498
- Michael J, Giannuzzi L (2007) Improved EBSD sample preparation via low energy Ga + FIB Ion milling. *Microsc Microanal* 13(S02):926–927
- Morawiec A, Field DP (1996) Rodrigues parameterization for orientation and misorientation distributions. *Philos Mag A* 73(4):1113–1130
- Nicolas A, Poirier J-P (1976) Crystalline plasticity and solid state flow in metamorphic rocks. *John Wiley & Sons, London*, p 444
- Nishikawa S, Kikuchi S (1928a) Diffraction of cathode rays by calcite. *Nature* 122(3080):726–726
- Nishikawa S, Kikuchi S (1928b) Diffraction of cathode rays by mica. *Nature* 121(3061):1019–1020
- Nolze G, Hielscher R (2016) IPF coloring of crystal orientation data. Preprint Technische Universität Chemnitz
- Nowell MM, Witt RA, True B (2005) EBSD sample preparation: techniques, tips, and tricks. *Microsc Microanal* 11(S02):504–505
- Passchier CW, Trouw RA (2005) *Microtectonics*, 2nd edn. Springer, Heidelberg
- Prakash M, Moon AP, Mondal K, Shekhar S (2015a) Effect of machining configurations on the electrochemical response of mild steel in 3.5% NaCl solution. *J Mater Eng Perform* 24(9):3643–3650
- Prakash M, Shekhar S, Moon A, Mondal K (2015b) Effect of machining configuration on the corrosion of mild steel. *J Mater Process Technol* 219:70–83
- Prior DJ (1999) Problems in determining the misorientation axes, for small angular misorientations, using electron backscatter diffraction in the SEM. *J Microsc* 195(3):217–225
- Raith M, Karmakar S, Brown M (1997) Ultra-high-temperature metamorphism and multistage decompressional evolution of sapphirine granulites from the Palni Hill Ranges, southern India. *J Metamorph Geol* 15(3):379–399
- Randle V (2004) Twinning-related grain boundary engineering. *Acta Mater* 52(14):4067–4081
- Randle V, Davies H, Cross I (2001) Grain boundary misorientation distributions. *Curr Opin Solid State Mater Sci* 5(1):3–8
- Reed BW, Kumar M (2006) Mathematical methods for analyzing highly-twinned grain boundary networks. *Scripta Mater* 54(6):1029–1033
- Reed BW, Minich RW, Rudd RE, Kumar M (2004) The structure of the cubic coincident site lattice rotation group. *Acta Crystallogr A* 60(3):263–277
- Sahu S, Sharma NK, Patel SK, Mondal K, Shekhar S (2019) The effect of grain boundary structure on sensitization behavior in a nickel-based superalloy. *J Mater Sci* 54:1797–1818
- Sahu S, Yadav PC, Shekhar S (2018) Use of hot rolling for generating low deviation twins and a disconnected random boundary network in inconel 600 alloy. *Metall Mater Trans A* 49(2):628–643
- Schwartz AJ, Kumar M, Adams BL, Field DP (eds) (2009) *Electron backscatter diffraction in materials science*, 2nd edn. Springer, US, Boston, MA, pp 21–143
- Sharma NK, Shekhar S (2017) Microstructure and property evolution for hot-rolled and cold-rolled austenitic stainless steel 316L. *Trans Indian Inst Met* 70(5):1277–1284
- Sharma NK, Shekhar S (2018) Deconvoluting error in measurement of low angle misorientation distribution. *Micron* 107:28–34
- Shekhar S, Abolghasem S, Basu S, Cai J, Shankar M (2012) Effect of severe plastic deformation in machining elucidated via rate-strain-microstructure mappings. *J Manuf Sci Eng* 134(3):031008
- Shoemaker K (1994) III.5.—Euler angle conversion. In: Heckbert PS (ed) *Graphics gems*, vol 4. Elsevier Inc, London, pp 222–229
- Singh S, Guo Y, Winiarski B, Burnett TL, Withers PJ, De Graef M (2018) High resolution low kV EBSD of heavily deformed and nanocrystalline Aluminium by dictionary-based indexing. *Sci Rep* 8(1):10991
- Stipp M, Tullis J (2003) The recrystallized grain size piezometer for quartz. *Geophys Res Lett* 30(21):2088
- Twiss RJ (1986) Variable sensitivity piezometric equations for dislocation density and subgrain diameter and their relevance to olivine and quartz. *Min Rock Deformation: Lab Stud, AGU Geophys Monogr* 36:247–263
- Vaid A, Mittal K, Sahu S, Shekhar S (2016) Controlled evolution of coincidence site lattice related grain boundaries. *Trans Indian Inst Met* 69(9):1745–1753
- Verma M (2014) Effect of machining configurations on the mechanical properties of SS316L. M.Tech. thesis at IIT Kanpur
- Wang YZ, Kong MG, Liu ZW, Lin CC, Zeng Y (2016) Effect of microscope parameter and specimen thickness of spatial resolution of transmission electron backscatter diffraction. *J Microsc* 264(1):34–40
- Wang Z, Saldana C, Basu S (2017) Subsurface microstructure and crystallographic texture in surface severe plastic deformation processes. In: *International manufacturing science and engineering conference*. American Society of Mechanical Engineers
- Watanabe T (1984) An approach to grain boundary design for strong and ductile polycrystals. *Res Mechanica* 11(1):47–84
- Wilkinson AJ (2001) A new method for determining small misorientations from electron back scatter diffraction patterns. *Scripta Mater* 44(10):2379–2385

- Wilkinson AJ, Britton TB (2012) Strains, planes, and EBSD in materials science. *Mater Today* 15(9):366–376
- Wilkinson AJ, Britton TB, Jiang J, Karamched PS (2014) A review of advances and challenges in EBSD strain mapping. *IOP Conf Ser: Mater Sci Eng* 55:012020
- Wilkinson AJ, Hirsch PB (1997) Electron diffraction based techniques in scanning electron microscopy of bulk materials. *Micron* 28(4):279–308
- Wilson AW, Spanos G (2001) Application of orientation imaging microscopy to study phase transformations in steels. *Mater Charact* 46(5):407–418
- Wright SI, Field DP, Nowell MM (2015) Post processing effects on GND calculations from EBSD-based orientation measurements. *IOP Conf Ser: Mater Sci Eng* 89:012049
- Wright S, Nowell M, Basinger J (2017) Precision of EBSD based orientation measurements. *Microsc Microanal* 17(S2):406–407
- Yadav PC, Sahu S, Subramaniam A, Shekhar S (2018) Effect of heat-treatment on microstructural evolution and mechanical behaviour of severely deformed Inconel 718. *Mater Sci Eng, A* 715:295–306
- Yadav PC, Sharma NK, Sahu S, Shekhar S (2019) Influence of short heat-treatment on microstructural and mechanical inhomogeneity of constrained groove pressed Cu-Zn alloy. *Mater Chem Phys* 238:121912
- Yadav PC, Sinhal A, Sahu S, Roy A, Shekhar S (2016) Microstructural inhomogeneity in constrained groove pressed Cu-Zn alloy sheet. *J Mater Eng Perform* 25(7):2604–2614
- Yuri T, Ono Y, Ogata T (2003) Effects of surface roughness and notch on fatigue properties for Ti–5Al–2.5Sn ELI alloy at cryogenic temperatures. *Sci Technol Adv Mater* 4(4):291–299
- Zaefferer S, Elhami N-N (2014) Theory and application of electron channelling contrast imaging under controlled diffraction conditions. *Acta Mater* 75:20–50